Alma Mater Studiorum · Università di Bologna

facoltà di scienze matematiche, fisiche e naturali
Corso di Laurea in Fisica del sistema Terra

Numerical and semi-analytical models of sliding masses : application to 1783 Scilla tsunamigenic landslide

Relatore:
Prof. S. Tinti

Correlatore:
Dt. F.Zaniboni

Presentata da:
Glauco Gallotti

Sessione invernale.
Anno accademico: 2013-2014

"*Scylla loco mansit.*
. . .mox eadem Teucras fuerat mersura carinas,
ni prius in scopulum, qui nunc quoque saxeus exstat,
transformata foret; scopulum quoque navita vitat."
The legend of Glaucus and Scylla, Ovidius

Contents

Abstract

The Scilla rock avalanche occurred on 6 February 1783 along the coast of the Calabria region (southern Italy), close to the Messina Strait. It was triggered by a mainshock of the "Terremoto delle Calabrie" seismic sequence, and it induced a tsunami wave responsible for more than 1500 casualties along the neighboring Marina Grande beach. The main goal of this work is the application of semi-analtycal and numerical models to simulate this event. The first one is a MATLAB code expressly created for this work that solves the equations of motion for sliding particles on a two-dimensional surface through a fourth-order Runge-Kutta method. The second one is a code developed by the Tsunami Research Team of the Department of Physics and Astronomy (DIFA) of the Bologna University that describes a slide as a chain of blocks able to interact while sliding down over a slope and adopts a Lagrangian point of view.
A wide description of landslide phenomena and in particular of landslides induced by earthquakes and with tsunamigenic potential is proposed in the first part of the work. Subsequently, the physical and mathematical background is presented; in particular, a detailed study on derivatives discratization is provided. Later on, a description of the dynamics of a point-mass sliding on a surface is proposed together with several applications of numerical and analytical models over ideal topographies. In the last part, the dynamics of points sliding on a surface and interacting with each other is proposed. Similarly, different application on an ideal topography are shown. Finally, the applications on the 1783 Scilla event are shown and discussed.

Chapter 1

Overview of Landslide Problems

1.1 Introduction

Landslides are important natural agents that shape mountainous areas and redistribute sediment in gentler terrain. Much of the present Earth's landscape has been extensively sculpted by episodic large landslides; more subtle, but significant modifications have also been made by frequent, smaller scale mass movements.
In general terms, we can define a landslide as a variety of processes that result in the downward movement of materials composed of natural rocks, soil, artificial fill, or combination of these materials. The displaced mass can move in a number of different ways: gravity is always the primary driving force, but it may be supplemented by water. Landslides differ from surface erosion processes, where water is the only driving mechanism.
The conditions that permit gravity to overcome the inertial forces of friction (that hold a slope together) include several kind of processes such as: variations in soil/rock water content, moisture levels, freezing of ice in jointed rock, seismic/volcanic activity or destabilizing human activities. Broadly speaking, heavy rains and earthquakes are the major landslides cause.
Several excellent summaries and books have been published on prediction, analysis, and control of landslides, particularly from an engineering or geotechnical perspective [*Turner and Schuster*,1996; *Abramson et al.*,2002;*Cornforth*,2005]. Additionally, several significant books have focused on specific landslide processes and environments [*Brunsden and Prior*,1984; *Eisbacher and Clague*,1984; *Dikau et al.*,1996].
Another important section of studies is focused on the hazard assessment and prediction methods. Essentially, methods of assessing landslide hazards can be roughly divided into four categories: terrain stability mapping [e.g.*Ives and Messerli*,1981; *Kienholz et al.*,1984;*Howes and Kenk*,1988]; simple rainfall-

landslides and earthquake-landslide relationship[e.g. *Caine*,1980; *Keefer et al.*,1987; *Larsen and Simon*,1933]; multi-factor, empirical landslide hazard assessments [e.g. *Gupta and Joshi*,1990; *Pachauri and Pant*,1992]; distributed, physically based models [e.g. *Miller*,1995; *Wu and Sidle*,1995].Some of these methods are more amenable to assessing relative landslide hazard at regional scales, others can be used as predictive tools for more specific sites, and yet others can be used to develop real-time warning system.
However, since this work is focused on the dynamics of a tsunamigenic landslide induced by an earthquake, the hazard assessment we'll not be treated in detail.

1.2 Classification System

To introduce the various classification systems, a brief description of landslides morphology is required.

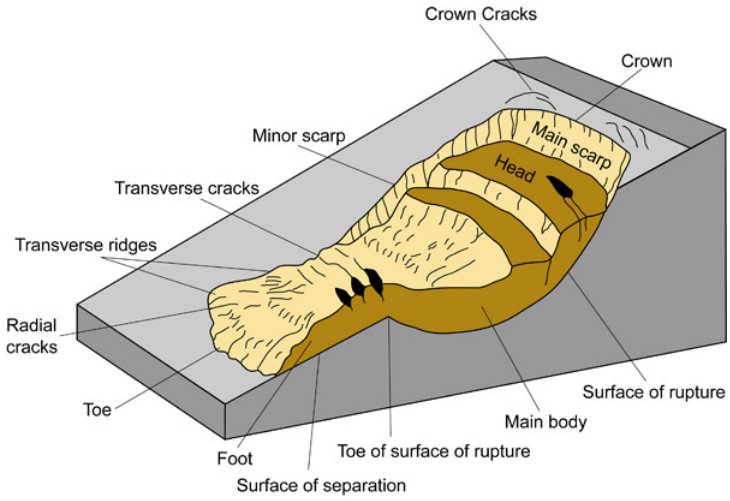

Figure 1.1: Schematic representation of a landslides. [Credit: *Idaho Geological Survey*]

As it's shown in figure 1.1 , we can define typical landslides characteristics:

1. **Crown**: the practically undisplaced material still in place and adjacent to the highest parts of the main scarp.

2. **Main scarp**: a steep surface on the undisturbed ground at the upper edge of the landslide, caused by movement of the displaced material away from the undisturbed ground.

3. **Top**: the highest point of contact between the displaced material and the main scarp.

4. **Minor scarp**: a steep surface on the displaced material of the landslide produced by differential movements within the displaced material.

5. **Main Body**: the part of the displaced material of the landslide that overlies the surface of rupture between the main scarp and the toe of the surface of rupture.

6. **Foot**: the portion of the landslide that has moved beyond the toe of the surface of rupture and overlies the original ground surface.

7. **Toe**: the lower, usually curved margin of the displaced material of a landslide, it is the most distant from the main scarp.

8. **Surface of Rupture**: the surface which forms (or which has formed) the lower boundary of the displaced material below the original ground surface.

9. **Toe of the Surface of Rupture** : the intersection (usually buried) between the lower part of the surface of rupture of a landslide and the original ground surface.

10. **Surface of Separation**: the part of the original ground surface overlain by the foot of the landslide.

Furthermore, geometrical characteristics of a landslides are generally defined as:

1. **Total length** L: the minimum length from the tip of the landslide to the crown.

2. **Total width** W: the distance among the landslide lateral border.

3. **Total depth** D: the maximum vertical length from the landslide summit to the sliding surface.

4. **Length of the displaced mass** L_d: minimum distance from the tip to the top.

5. **Width of the displaced mass** W_d: maximum breadth of the displaced mass perpendicular to the length of the displaced mass.

6. **Depth of the displaced mass**: the maximum depth of the displaced mass, measured perpendicular to the plane containing W_d and L_d.

From a geological point of view, several materials and soil characterizations have been defined. Since we are focused mainly on the landslide dynamics, a detailed description of these aspects we'll not be proposed.
Essentially, a classification system can be taxonomic, implying a hierarchy of descriptors to form a branch-like structure, or it can be a filing system. In this case, different items are placed into classes on the basis of various attributes. Otherwise, a typological classification is particularly useful . This is based on selected features and it's designed to present solutions at the problem at hand.

Taxonomy is difficult to achieve due to the uncertainties related to the process mechanism in many landslides phenomena. Since the main goal with landslides is to solve problems (like the hazard assessments) , typological classification appears to be the most useful one.
Slope movements have been classified in many ways, with each method having some particular usefulness or applicability related to the recognition, avoidance, control or correction of the hazard. *Sharpe*[1938] proposed a comprehensive scheme for classyfying mass wasting based on geomorphology in which processes were divided into four categories:

1. **Slow-flowage types**: creep and solifluction.
2. **Rapid-flowage types**: earthflows, mudflows and debris avalances.
3. **Landslides**: slumps, debris slides, debris falls, rockslides and rockfalls.
4. **Subsidence.**

On the other hand, the widely used classfication, *Varnes*[1978] (figure 1.2) distinguish five types of mass movements:

1. **Falls**: the sliding mass is actually free to fall over a steep slope. Velocity range can reach values of a free falling body.
2. **Topples**: rotational motion of rock blocks around a hub collocated under the blocks or on the blocks base. The motion is generally gravity induced. The dimensions can reach considerable values (up to $10^6 m$).
3. **Slides**: movement parallel to planes of weakness and occasionally parallel to slope. The motion is caused by shear stresses acting on inward surfaces. Generally, two types of slides are defined: rotational and translational . In the first ones the failure plane is typically concave and the movement is extremely slow (less than $1m/day$). The second ones occur on existent disruption surfaces with an inclination equal (or lower) to the slope one. The sliding mass can go through lots of kilometers, reaching velocity of $50m/s$ in the rocks slide.
4. **Spreads**: huge lateral motion over a plastic-like surfaces. The movement is generally slow($1m/10min$ - $1m/day$)
5. **Flows**: viscous to fluid-like motion.

Other classes are defined as combinations of these principal types along with the type of material : bedrock (rock underlying the surface), coarse soils and predominately fine soils. Further subdivision is based on speed of movement.
When a landslide passes through several phases as it progresses downslope it can be considered *complex*, even if one type usually predominates in different parts of the moving mass or at different times during the period of displacement.
Several modifications of the original *Varnes*[1978] have been made: [*Cruden and Varnes*,1996,*Brunsden*,1985;

Hutchinson,1988]. This kind of classification is weakly taxonomic.

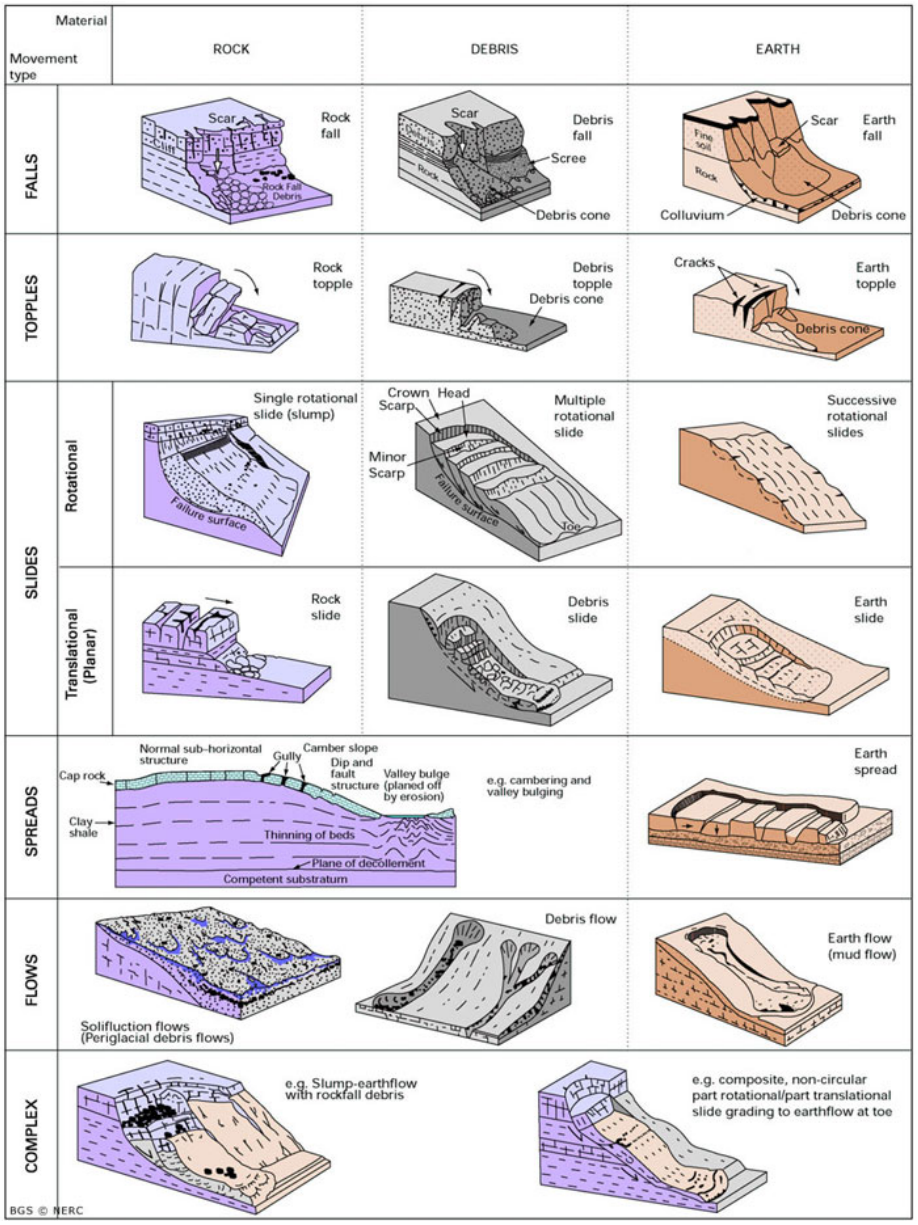

Figure 1.2: *Varnes*[1978] landslide classification system.[Credit: *British Geological Survey*]

Keefer[1984] employed similar principles and terminology as *Varnes*[1978] to classify earthquake-induced landslides based on material type (soil or rock), type of movement(disrupted or coherent), and other characteristics (e.g. velocity, depth, water content). This classification includes three main categories of landslides:

1. **Disrupted slides and falls.**
2. **Coherent slides** (e.g. slumps, earthflows)
3. **Lateral spreads and flows.**

Moreover, based on the frequency of occurrence during 40 earthquakes ($M5.2$ to 9.2), *Keefer*[1984] categorized landslides as very abundant ($> 2500\,event^{-1}$), abundant ($250 - 2500\,event^{-1}$), and uncommon.
Obviously, limitations exists for any type of classifications. For example, *Cruden and Varnes*[1996] use the prehistoric Blackhawk landslide in the San Bernadino Mountains of southern California as a case of significant mass movement that is difficult to classify according to their system. Additionally, their system, among others, employs an elaborate set of descriptors that, while informative for engineering geologists, may be confusing for land managers dealing with slope stability. For the purposes of assessing the effect of land management in potentially unstable terrain as the degree of landslide risk, the most important aspects to consider are: the size of the landslide(typically given by depth to the failure plane) , the rate of movement response to climate and earthquakes and the sensitivity to various anthropogenic disturbances (e.g. climate change, vegetation modification).
The classifications system we introduced have been developed from either geomorphological or geotechnical perspectives . Intrinsically, these system provide detailed descriptions of the mode of failure, materials, velocity and failure mechanism of landslides. To have a rather simple categorization of soil mass movements, *Sidle and Dhakal*[2002] proposed another classification that recognize the importance of combinations of mass displacements and follows the terminology employed by *Varnes*[1978] as much as possible. Five functional categories of mass movements are described:

1. **Shallow , rapid landslides** . Debris slides and avalanches are typical shallow movement types in steep (> 25 gradient) terrain. Soil are characteristically $< 2m$ deep and have low cohesive properties. The shallow soil mantle overlies either bedrock or another permeability layer (e.g., glacial or marine till) that acts as failure plane. This plane is generally oriented parallel to the soil surface, allowing the use of the infinite slope model. This landslides are typically longer than their width and have length do depth ratio < 0.1 [*Wentwoth*,1943; *Skempton and Hutchinson*,1969;*Cruden and Varnes*,1996] and initiate on slopes that are typically either concave or linear in plan form[*Swanston*,1969; *Gao*,1993; *Palacious et al.*,2003]. Sequence of linked debris slides, avalanches, and flows are major sources of sedimentation in mountain streams. Typically, this kind of landslides are

generally triggered by rainstorms, rapid snowmelt, earthquakes, or combinations of these factors. Also lahar (debris flow that initiate on volcanic slopes in recently deposited ash or debris) belong to this category (figure 1).

Figure 1.3: Lahar formed after 1982 Mount St. Helens eruption in Washington state as an example of shallow and rapid landslides. (Credit: *Tom Casadevall*,USGS)

2. **Rapid, deep slides and flows.** Rapid, deep slides and flows include large debris slides, debris flow, dry flows, bedrock slides and certain block glides and rapid earthflows. Some of the terrain and material characteristics are similar to those of shallow, rapid landslides but responses to triggering factors often differ. Anyway, the main difference with respect to the previous category is the slide thick ($> 5m$). Furthermore, the sliding mass often include a significant proportion of weathered or fractured bedrock. The main trigger mechanism are typically long rainfall periods or strong earthquakes. In fact, strong ground motion is sometimes required to initiate failures in deeper regoliths [e.g., *Shoaei and Ghayoumian*,2000].

3. **Slower, deep-seated landslides**. The deep-seated landslides include slumps, earthflows and lateral spreads that move at rates generally $< 1m\,day^{-1}$. Both active and dormant slides characteristically occur in gently sloping topography that is often hummocky with immature drainage system [*Swanson and Swanston*,1977; *Bechini*,1993; *Ocakoglu et al.*,2002].

Failure occurs in deep, heavily weathered clay-rich soils or regoliths that exhibit plastic behavior over a range of water contents. Slumps and earthflows are quite often a coupled phenomena: the initial movement is typically a rotational slumps, and subsequent downslope movement of the mass is by earthflow [e.g., *Okunishi*,1982; *Rohn et al.*,2003]. The dimensions of these displacements are generally larger than shallow rapid landslides and move in response to seasonal or at least multi-day accretion of groundwater related to inputs from rainfall or snowmelt: once a critical level of groundwater is present, movement accelerates rapidly [*Campbell*,1966;*Furuya et al.*,1999; *Coe et al.*,2003]. It's important to underline that, despite their slower rates, deep-seated mass movements are responsable for the transport of large volumes of sediment to streams and rivers in certain regions [*Sasaki et al.*,2000].
Lateral spreads (figure 3) can be defined as the lateral displacement of a large mass of cohesive rock or soil overlying a deforming mass of soft materials [*Dikau et al.*,2000; *Varnes*,1996]. Movement is initiated by high internal pore water pressure from rainfall or snowmelt or by earthquakes[*Asch.,1996*].

Figure 1.4: Lateral spreads in Anchorage, Alaska, caused my the Great Alaska Earthquake ($M = 9.2$) as an example of slower, deep-seated landslides. (Credit: *A. Grantz.*,USGS)

4. **Slow flows and deformations**. These displacement occur in terms of

soil creep that is not properly a failure per se, but a plastic deformation of the soil mantle. Active soil creep are often associated with slump-earthflow; thus, terrain characteristic are the same. Movement rates typically decrease with depth [*Swanston*,1981; *Sonoda*,1998] and have values of the order of millimeters per year.

5. **Surficial mass wasting**. This motion is generally not considered together with landslides; however, it is a gravity-driven process that is technically a mass movement. In fact, dry ravel and dry creep belong to this category even if they are superficial processes. They involve the downslope of individual soil grains, aggregates, and coarse fragments by rolling, sliding or bounding. The main cause of these mechanisms can be found in the loss of interlocking frictional resistence among soil aggregates or grains [e.g.*Hough*,1951;*Rahn*,1969]. These are a less perceptible type of erosion and usually transport far less sediment compared to other mass wasting processes.

1.3 Earthquake-induced landslides

There are several natural factors influencing landslides but we'll focus our attention mainly on seismicity. Earthquake-induced landslides are not very common, so there have been few opportunities to study the mechanism of the former. However, studies have shown that they often occur in convex topography because convex landforms respond strongly to earthquake motion [e.g., *Harp et al.*,1981; *Murphy*,1995; *Okunishi et al.*,1999]. It's generally very difficult to associate earthquake-induced motion to landslide mass displacement because quakes exert very complex stresses on slopes since the seismic loads vary dynamically. Virtually, all types of landslides can be associated with different magnitude earthquakes in various settings. Furthermore, quakes can also reactivate dormant or slow-moving landslides.
From a physical point of view, the propagation of seismic waves causes a horizontal acceleration of the soil mantle. The cyclic loading and unloading of soils during earthquakes depends on many factors and exert major stress that can causes landslides. Moreover, cycling loading of regoliths may generate high pore water pressures that trigger landslides [*Seedand Lee*,1966; *Wu and Sangrey*,1978; *Ochiai et al.*,1985].
Many factors related to earthquakes and the settings in which they propagate affect the number, sizes and types of landslides. Even if the intrinsic physics features of the earthquake (magnitude, focal depth, etc.) are fundamental, factors related to the environments in which the shake occur are essential. The most crucial are:

1. Inert stability of the potential failure sites.
2. Existence of old or dormant landslides.
3. Vegetation and land use.

4. Orientation of potential failures in relation to the earthquake epicenter.

5. Orientation of existing faults with respect to the direction of seismic wave propagation.

6. Regolith wetness.

7. Slope gradient and other topographic factors.

All these factors, at least at some degree, are quite difficult to separate. Broadly speaking, rock falls, rock slides, soil falls and disrupted soil slides are triggered by the weakest seismic activity; deep-seated slumps and earthflows are generally initiated by stronger (and probably of longer duration) seismic activity; lateral spreads, debris flows and subaqueous landslides require the greatest seismic activity [*Keefer*,1984,2002]. Compared to other land shapes, convex land form exhibit stronger seismic amplification. Particulary, mountain ridges shake strongly during earthquake and shear failure may occur on these slopes, triggering a landslide [*Harp and Gibson*, 1996; *Tang and Grunert*, 1999; *Khazai and Sitar*, 2003]. This particular phenomenon is generally called topographic effect. Studies have demonstrated that significant amplification occurs when the wavelength of the seismic wave is the same as the length of the land shape [*Boore*, 1973; *Nishimura and Morii*, 1983]. Intensification of ground acceleration by as much as 75% can occur, but in areas of complex topography the overall influence of ground motion cannot be easily predicted. Evidences have shown that scarp that faced away the direction of oncoming seismic waves are most prone to landslides. In other cases, large topographic effects have been observed at sites where slope gradient changed and on convex land shape along streams. [*Harp et al.*, 1981]. However, in spite of the many empirical investigations that associate topographic effects with earthquake-induced landslides, the degree to which such effects amplify seismic motion and the influence of this amplified motion on the resultant stress have yet to be clarified, due to the lack of detailed seismic observations in mountainous areas. Hence, to determine the degree of the topographic effect, behavior of slopes during an earthquake was quantitatively modeled to estimate the acceleration response [*Ochiai et al.*, 1995]. Results have proved that a large response to the acceleration waveform input was observed from the bottom of the model in a direction orthogonal to the ridge line. Furthermore, the amplification can be caused also by the contact of jointed rock masses [*Li et al.*,2000; *Rovelli et al.*,2002; *Martino et al.*,2006].Based on seismometric records, this effect can be identified in terms of: monofrequancial wave packages of recorded earthquakes; clear frequency peaks in both horizontal to vertical spectral ratios and site-to-reference spectral ratios; directional effects in energy azimuthal distribution.
Another factor influencing earthquake-induced landslides is represented purely by geologic aspects. Some studies have shown the possibility of landslide initiation due to liquefaction of pumice layers based on a stability analysis of a gradual slope [*Ochiai et al.*, 1985]. In some areas of Japan and southern Italy, numerous earthquake-induced landslides occurred in weathered and foliated rocks formed

mainly by quartz and mica ('biotite gneiss') [*Murphy*, 1995]. Moreover, many studies have noted the susceptibility of poorly consolidated sedimentary rocks and sediments to landslides during earthquakes.

1.4 Tsunamigenic landslide

Tsunamis are a particular type of long waves induced by a strong and quick impulse that can propagate in a ocean basin also for long distances.
Basically, tsunami waves are generated by a rapid displacement or motion of large volumes of water. The main sources of such events are normal faulting of earth plates during submarine earthquakes, volcanic eruptions or subaerial and submerged landslides. The tsunami wavelength in deep waters can be very considerable (hundreds of kilometers) with respect to its elevation (few centimeters up to one meter)and its velocity is of the order of hundreds of kilometers. Hence, when the wave approaches shallower waters, due to mass and energy conservation, it slow down and increases its elevation. Due to its time and space scale , it's easy to imagine how potentially destructive and dangerous this phenomenon can be.
Since the focus of this study is the dynamic of a tsunamigenic landslide, we'll describe in detail only the mechanism of impulse waves generated by sub-aerial landslides. Actually, there are few documented cases of large subaerial landslides falling into water and causing large localized impulse waves. One of the most spectacular examples was the Lituya Bay (Alaska) landslide on July $10, 1958$. The landslide, triggered by an earthquake, fell into a narrow fjord and caused a wave that reached a maximum height of $520m$. However, when the wave reached the open ocean, its amplitude diminished quickly [e.g., *Miller*, 1960]. The Vajont reservoir disaster in 1963 [*Muller*, 1964;*Trollope*, 1980; *Zaniboni, Paparo, Tinti*, 2013] represents another event of this nature. Despite the landslide amplitude, the following three stages in the evolution of the landslide generating tsunami can be distinguished:

1. **Triggering of slope failure.**
2. **Post failure landslides.**
3. **Tsunami generation and propagation.**

Slope failure (stage I) occurs primarily on open continental-margin slopes and in the active river deltas in under,and normally consolidated, sandy and clayey sediments. At the onset of stage II, when the slide breaks out, the moving landslide generates the tsunami wave. Subsequently to the sliding process, some landslides mobilize into flows and turbidity currents, whereas others remain slides or slumps with limited deformations and displacements [*Locat and Lee*, 2002]. During stage III, the water wave propagates through the water towards the shore. Commonly, three different boundary value problems for the analysis of the tsunami wave are distinguished: wave generation at the source ;wave

propagation in the open water ;wave run-up along the continental slope into the shore. While stages II and III of the evolution process are usually viewed as dynamic processes, conventional analysis of the slope failure (stage I) focuses commonly on the final limiting equilibrium state, which is a static condition.
Researchers have been studying the process of tsunami generation by submarine and subaerial landslides both analytically and numerically [*Harbitz*, 1992; *Pelinovsky and Poplavsky*, 1996; *Ward*, 2001; *Tinti et al.*, 1997; *Satake*, 2001;*Murty*, 2003; *Dutykh and Dias*, 2009].

In order to explain higher maximum velocities, models accounting for the initial acceleration from earthquakes have been developed [e.g., *Harbitz*, 1992]. However it is known that this is not always legitimate. For instance, in the Aitape 1998 event , the submerged landslide occurred some $10 - 15min$ after the earthquake [*Davies et al.*, 2003]. Consequently, earthquake acceleration cannot always explain an initial landslide velocity.
However, the whole process is complex and, as we have seen in the previous section, depends on several kind of factors, both physical and geological.

1.5 Scilla 1783 event

The Scilla (Calabria region, Italy) rock avalanche is one of the main ground effects induced by the 1783 "Terremoto delle Calabrie" seismic sequence [*Boschi*, 2000] and represent one of the most damaging landslides in the Italian history. The sequence struck the southern part of Calabria region between February $5th$ and March $28th$ 1783 and it was characterized by five main shocks, with magnitude among 5.8 and 7.3 . All these earthquakes resulted to be tsunamigenic, though the size of the generated tsunamis differed very much case to case. Furthermore, due to it's relevant time scale and relatively small space scale this process leads to several cumulative effects, bringing great changes in the environment morphology.

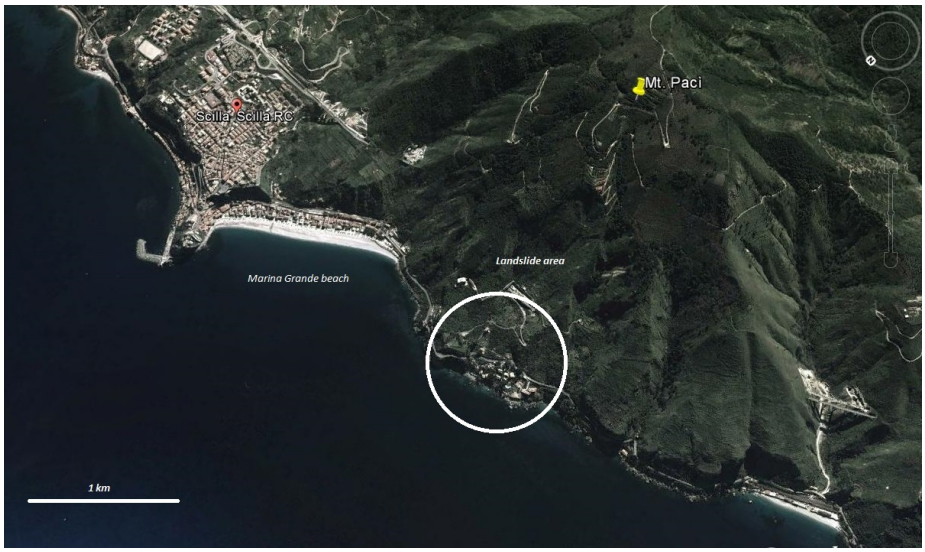

Figure 1.5: Location of Mt.Pací and approximate landslide area. Credit[*Google earth*,2015]

The Scilla event occurred on $6th$ February 1783 at $1:45$ a.m. in the Mt. Pacı' coastal slope (figure 1.5, located few kilometers away from the Scilla village. The terrain collapse took place some 30min after an earthquake with an estimated surface magnitude of 5.8 [*Sarconi*,1784; *De Lorenzo*, 1877; *Minasi*, 1970-1971]. The rock mass fell into the sea as a rock avalanche, inducing a huge tsunami, as high as $16m$, that killed more then 1500 inhabitants along the Marina Grande beach [*Hamilton*, 1783;*Sarconi*,1684; *Minasi*, 1785; *Vivenzio*, 1788; *De Lorenzo*, 1877]. The Mt.Pací slope is quite steep (up to 45) and intensely jointed gneiss rock and breccias crop out extensively [*Bozzano et al.*, 2008; *Mazzanti*, 2008]. The landslide was bounded by two faults in the upper and lower part of the scar area and laterally confined (in the left part) by a major regional fault. Actually, this particular geological set represented both a predisposing factor and kinematic control for the 1783 event. In fact, it is suggested that rock avalanche it's been induced by the failure of a wedge of rock, due to the fragmentation of the jointed rock mass and to the slope morphology [*Bozzano et al.*, 2008-2010; *Mazzanti*, 2008]. For this reason we can consider the landslide as complex, in the [*Varnes*, 1978] classification system.
The subaerial volume of the displaced mass has been calculated as the difference among a hypothetical pre-landslide morphology and the present one by reshaping the slope based on both geomorphological features and engravings by [*A. Minasi*, 1970].

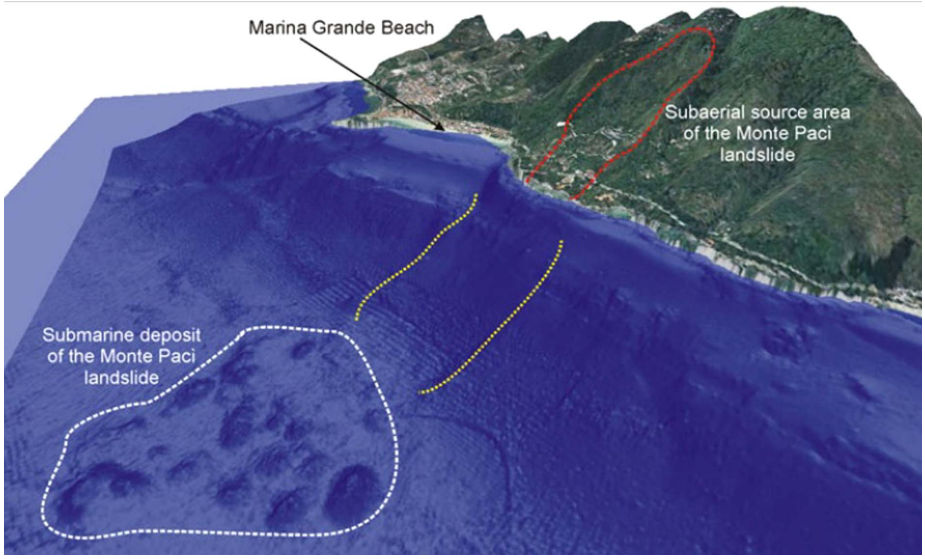

Figure 1.6: 3D view of Mt. Pací and Scilla coastal line.The with dashed line bounds the 1783 mandslide deposit. The red dashed line point out the subaerial landslide. The yellow dotted lines underline the lateral boundaries of the submarine depression. Source: art[2]

Thanks to the submarine geophysical investigations [*Bosman et al.*, 2006], a large submarine depression close to the toe of the subaerial scar it's been recognized. (figure 1.5). Moreover, a huge depositional bulge with hummocky morphology was identified just at the toe of the submarine depression, and it has been interpreted as the landslide deposit. The maximum deposit depth is of the order of $15m$. In a distance of $1.7km$ from the coast line, large blocks (volumes between 100 and $200.000m^3$) randomly distributed have been detected. Anyway, the landslide accumulation is widely spread over a relatively flat seafloor and covers an area of about $1km^2$. Hence, an estimated landslide volume of $9.4 \times 10^6 m^3$ seems comparable with the total volume of the deposit.
Analysis of the correlation between the subaerial and submarine depression suggest that they occured as two separate events [*Mazzanti*, 2008]. Evidence from HR Multybeam Bathymetry in the conjunction zone between the subaerial and the submarine scars suggest that the submarine landslide occured before the 1783. Anyway, in this work we consider only the subaerial landslide and its collapse into the water that leads to the tsunami generation.
In several studies [*Tinti and Guidoboni*, 1988; *Tinti et al.*, 2004; *Graziani et al.*, 2006; *Gerardi et al.*, 2008] it's shown how the February $6th$ tsunami at Scilla was induced by the Mt. Pací landslide. The time sequence of the earthquake, landslide and tsunami can be seen as the first clear evidence of a landslide source for the tsunami. As a matter of fact, according to historical reconstruction, the landslide occurred 30 minutes after the shock and the tsunami hit the close

Marina Grande beach after 30-60 seconds after the landslide. Moreover, the corresponding wave height distribution in the area nearby the landslide, confirm the landslide origin of the tsunami. Maximum run-up heights ranging from $6 \text{to} 9m$ according to [*Sarconi*, 1784] and up to $16m$, according to [*Minasi*,1785] were recorded along the Marina Grande beach. Going further from the source, the wave run-up acutely decrease: Chianalea (Sicily) $5-6m$; Cannitello (Sicily) $0.8-2.9m$; Catona (Sicily) $0.3-0.7m$.

Chapter 2

Physical and mathematical background

2.1 Differential equations

A differential equation relates a function with its derivatives. Hence, the solution will be a function, or a class of functions, not a number. From a physical point of view, if the equation describes the time evolution of a process, it relates quantities characterizing the process with their rate of change. Basically, most kinds of physical processes are described by means of differential equations
An ordinary differential equation (ODE) problem is defined as:

$$\frac{du}{dt} = f(u,t) \qquad u(t=0) = u_0 \tag{2.1}$$

where $u = u(t)$ is a general variable, f is a continuous function and du/dt indicates the total derivative of u with respect to the time t. We can distinguish different kinds of ODE, depending on the f shape. A linear ODE occurs when $f(u,t) = A(t)u + B(t)$ and it is well known that its solutions form a linear space, since the sum of any set of solutions or multiples of solutions is also a solution. Homogeneous ODEs are a further subclass for which $B(t) = 0$ and therefore the ODE takes the form $f(u,t) = A(t)\,u$
In the ODE general form u is an array formed by n components, so we have a system composed by n equations like the **??**. An important aspect of this kind of equations is that we can always re-write any differential equation with derivatives of higher order in this form including only functions and first-order derivatives. To have a clear understanding of this kind of equations, let us consider the following example:

$$\begin{cases} u_t = Au \\ u(t=0) = u_0 \end{cases} \tag{2.2}$$

where u_t indicates the derivative of u with respect to t, and A is a constant. It is well known that the solution of the above problem, that specifies an initial condition and is called a Cauchy problem, is $u(t) = u_0 \exp(At))$. In particular, the solution to any Cauchy problem exists and is unique only if: u is continuous and can be derived, f is continuous in the t variable and uniformly continuous in the u one. Calling D the domain of definition, the last condition is always satisfied if: $\forall u, v \in D, \quad \exists M$:

$$\parallel f(u,t) - f(v,t) \parallel < M \parallel u - v \parallel$$

When we are dealing with more complex systems, quite often we have to link different variables together and with their rates of change. Formally, we relate unknown multi-variable functions and their partial derivatives. In this case the equations are called "Partial differential equation" (PDE). A part from the presence of multi-variable functions, the main difference with the ODE is that we have to know not only initial conditions, but also boundary conditions. To show the PDE properties let us consider the example of the heat diffusion equation in the simplest possible form where only one space coordinate is involved: i.e.:

$$\frac{\partial u}{\partial t} = b^2 \frac{\partial^2 u}{\partial x^2} \qquad u(x, t = 0) = u_0(x) \tag{2.3}$$

where $u = u(x,t)$ is the temperature, $\partial u/\partial *$ indicates the partial derivatives whit respect to $*$and b is the thermal diffusivity. Let us further assume that the solution belongs to the domain $[-L/2, +L/2]$, with $L \in Re$. If we impose the initial condition $u_0(x) = U \cos(\frac{\pi}{L}x)$ and the boundary condition $u(\pm L/2, t) = 0$, and if we suppose that the solution has the form:

$$u^{\alpha}(x,t) = U \cos(\frac{\pi}{L}x)\, e^{-\alpha t}$$

which automatically satisfies the initial condition as well as the conditions at the boundaries, we can easily find the exact solution to be:

$$u(x,t) = U \cos(\frac{\pi L}{x})\, e^{-\frac{\pi^2 b^2 t}{L^2}} \tag{2.4}$$

This example clearly shows the need of specifying boundary conditions in addition to initial condition in order to identify univocally a solution for a PDE.

2.2 Numerical Methods

Analytical solutions like the ones given in the previous very simple examples exist only for few particular cases, and hence some general way of finding solutions to problems based on differential equations has to be introduced. The key for solving every kind of problem is *discretization*, that is the process of transferring continuous models and equations into discrete counterparts. Solutions computed with this process are called numerical.

Firstly, let us consider an ODE. In this case we have to *discretize* only the time axis. Choosing a specific time step $\Delta t = k$, we can represent the time by means of a sequence of equally spaced instants $t_n = nk$ and search for an approximate solving sequence $v^n \approx u(t_n)$, with the first-step value being given by $v^0 = u_0 = u(t = 0)$. Expanding the u time derivative we find:

$$\frac{\partial u}{\partial t}(t_n) = \lim_{\Delta t \to 0} = \frac{u(t_n + k) - u(t_n)}{k} = \frac{v^{n+k} - v^n}{k} = f(v^n, t_n) = f^n$$

Taking this into account, we are able to define the most elementary discretization method, that is named Euler method:

$$\begin{cases} v^{n+1} = v^n + kf^n \\ v^0 = u_0 \end{cases}$$

This method is explicit because it uses variables of the previous step n to evaluate variables at the next one n+1. The implicit version of the method has the form:

$$\begin{cases} v^{n+1} = v^n + kf^{n+1} \\ v^0 = u_0 \end{cases}$$

There are several kinds of formulas that provide different approximate solutions. Among these special relevance have the so-called linear multi-step methods, such as the Adams-Bashforth's (explicit) and the Adams-Moulton's (implicit) formulas that can be given the following general forms respectively:

$$A.B. \qquad v^{n+1} = v^n + k(\alpha_0 f^n + \alpha_1 f^{n-1} + \alpha_2 F f^{n-2} ... + \alpha_{s-1} f^{n+1-s}) \quad (2.5)$$

$$A.M. \qquad v^{n+1} = v^n + k(\alpha_{-1} f^{n+1} + \alpha_0 f^n + \alpha_1 f^{n-1} ... + \alpha_{s-1} f^{n+1-s}) \quad (2.6)$$

where α_i are numerical coefficients. Notice that these methods cannot be applied in the first steps since one has to know the values f^{n-1}, f^{n-2}... that can be evaluated by iterating the Euler formula.

2.2.1 Runge-Kutta discretization methods

Another kind of methods that provide a very useful discretiazation are due to the work of the German mathematicians C. Runge and M. W. Kutta. and are universally known as Runge-Kutta methods. We will denote them as RK methods. It is worth stressing that the equations of motion for the landslide problem that is the key-topic of this work have been solved via one of such methods.
Differently from the multistep approaches, the RK methods take into account only one single time step. The simplest RK method can be introduced as follows. Let us focus our attention on the time step $[t_n, t_{n+1}]$ and integrate both members of the equation **??** over this time interval. Hence we get :

$$v^{n+1} = v^n + \int_{t_n}^{t_{n+1}} f(u, t)\, dt \quad (2.7)$$

Further, let us introduce some intermediate temporary values (designated by means of the symbol $\sim$) :

$$\tilde{v}^{n+1/2} = v^n + k/2\, f^n \Rightarrow \tilde{f}^{n+1/2} = f(\tilde{v}^{n+1/2}, t_{n+1/2})$$

If we approximate the integral in 2.7 by the product of Δt times the mean value of f in the interval $[t_n, t_{n+1}]$, we obtain the final formula:

$$v^{n+1} = v^n + k\tilde{f}^{n+1/2}$$

In the general approach, we introduce, in the step $[t_n, t_{n+1}]$, a number of intermediate values in correspondence of the s times t_{n+c_i}, with $0 < c_i < 1$ and $c_1 = 0$. Basically, the procedure can be written in the form:

$$\begin{array}{ll} v^n \to v^{n+c_2} = v^n + k\alpha_{21}\tilde{f}^n & \Rightarrow \tilde{f}^{n+c_2} = f(\tilde{v}^{n+c_2}, t_{n+c_2}) \\ \tilde{v}^{n+c_3} = v^n + k\,(\alpha_{31} f^n + \alpha_{32}\tilde{f}^{n+c_2}) & \Rightarrow \tilde{f}^{n+c_3} = f(\tilde{v}^{n+c_3}, t_{n+c_3}) \end{array}$$

$$\vdots$$

$$\tilde{v}^{n+c_s} = \ldots = \tilde{f}^{n+c_s} = f(\tilde{v}^{n+c_s}, t_{n+c_s})$$

Using the s intermediate values of f, we can write:

$$v^{n+1} = v^n + k\,(\beta_1\tilde{f}^n + \beta_2\tilde{f}^{n+c_2} + \ldots + \beta_s\tilde{f}^{n+c_s}) \tag{2.8}$$

We refer to 2.8 as Runge-Kutta s-order explicit method.
Hence, to specify a particular method, one needs to provide the integer s (the number of stages), and the coefficients α_{ij} (for $1 \le j < i \le s$), b_i (for $i = 1, 2, \ldots, s$) and c_i (for $i = 2, 3, \ldots, s$). The matrix $[\alpha_{ij}]$ is called the Runge-Kutta matrix, while the coefficients b_i and c_i are known as the weights and the nodes [*Iserles, Arieh*, 1996]. These data are usually arranged in a mnemonic device, known as a *Butcher* matrix:

$$\begin{array}{c|ccc} c_1 = 0 & & & \\ c_2 & \alpha_{21} & & \\ c_3 & \alpha_{31} & \alpha_{32} & \\ \vdots & \vdots & \ddots & \\ c_s & \alpha_{s1} & \ldots & \alpha_{s\,s-1} \\ \hline & b_1 & \ldots & b_s \end{array}$$

The method is consistent if:

$$\sum_{j=1}^{i-1} \alpha_{ij} = c_i$$

2.3 Derivative discretization

These discretization formulas can be proven to be either exact for a limited class of functions or to be accurate up to the first order in the ratio $h/(x-x_0)$ or $k/(y-y_0)$, where x_0 and y_0 are zeros of the corresponding function derivatives, which means that the relative errors have order of magnitude of $(h/(x-x_0))^2$ and $(k/(y-y_0))^2$ respectively. To verify this accuracy, a comparison between derivatives estimated trough 2.9−2.13 and their analytical expressions was made by considering a large number of functions $f(x,y)$. Of all of these cases, for the sake of brevity we present here only one example in the following. A fourth-degree polynomial function has been chosen of the form:

$$\delta_+ V_i^j = \frac{V_{i+1}^j - V_i^j}{k} \qquad \delta^+ V_i^j = \frac{V_i^{j+1} - V_i^j}{h}$$

$$\delta_- V_i^j = \frac{V_i^j - V_{i-1}^j}{k} \qquad \delta^- V_i^j = \frac{V_i^j - V_i^{j-1}}{h}$$

where V_i^j is an approximation of the value $f(x_i, y_j)$. In terms of the above expressions, we can write:

$$\begin{aligned} f_x &= \frac{1}{2}(\delta_+ + \delta_-)V_i^j \\ &= (V_{i+1}^j - V_{i-1}^j)\frac{1}{2k} \end{aligned} \tag{2.9}$$

$$\begin{aligned} f_y &= \frac{1}{2}(\delta^+ + \delta^-)V_i^j \\ &= (V_i^{j+1} - V_i^{j-1})\frac{1}{2h} \end{aligned} \tag{2.10}$$

$$\begin{aligned} f_{xx} &= \frac{1}{2}(\delta_+(\delta_- V_i^j) + \delta_-(\delta_+ V_i^j)) \\ &= \delta_+(\delta_- V_i^j) \\ &= \delta_+ \frac{(V_i^j - V_{i-1}^j)}{k} \\ &= \frac{V_{i+1}^j - V_i^j - V_i^j + V_{i-1}^j}{k^2} \\ &= \frac{V_{i+1}^j - 2V_i^j + V_{i-1}^j}{k^2} \end{aligned} \tag{2.11}$$

$$
\begin{aligned}
f_{yy} &= \frac{1}{2}(\delta^+(\delta^- V_i^j) + \delta^-(\delta^+ V_i^j)) \qquad (2.12)\\
&= \delta_+(\delta_- V_i^j)\\
&= \delta^+ \frac{(V_i^j - V_i^{j-1})}{k}\\
&= \frac{V_i^{j+1} - V_i^j - V_i^j + V_i^{j-1}}{h^2}\\
&= \frac{V_i^{j+1} - 2V_i^j + V_i^{j-1}}{h^2}
\end{aligned}
$$

$$
\begin{aligned}
f_{xy} &= \frac{1}{4}(\delta^+(\delta_+ V_i^j) + \delta^+(\delta_- V_i^j) + \delta^-(\delta_+ V_i^j) + \delta^-(\delta_- V_i^j)) \qquad (2.13)\\
&= \frac{V_{i+1}^{j+1} - V_{i+1}^{j-1} - V_{i-1}^{j+1} + V_{i-1}^{j-1}}{4kh}
\end{aligned}
$$

These discretization formulas can be proven to be either exact for a limited class of functions or to be accurate up to the first order in h/x or k/y, which means that the relative errors have order of magnitude of $(h/x)^2$ and $(k/y)^2$ respectively. To verify this accuracy, a comparison between derivatives estimated trough 2.9−2.13 and their analytic expressions was made by considering a large number of functions $f(x, y)$. Of all of these cases, for the sake of brevity we present here only one example in the following. A fourth-degree polynomial function has been chosen of the form:

$$f(x, y) = ax^4 + by^4 + cxy + dx^2 + ey^2 + f \qquad (2.14)$$

Where $a = 0.2, b = 0.3, c = 0.5, d = 0.2, e = 0.07, f = 10$, and z has to be considered as given in meters. The analytic derivatives are:

$$f_x = 4ax^3 + cy + 2dx \quad f_y = 4by^3 + cx + 2ey$$

$$f_{xx} = 12ax^2 + 2d \quad f_{yy} = 12by^2 + 2e \quad f_{xy} = 2c$$

Through a MATLAB code, we have computed the discrete and analytic derivatives. Calling f_i^{dis} the discrete ones, and f_i^{an} the analytic ones, the percentage absolute error was estimated by means of the formula

$$E = 100 \times \frac{|f_i^{dis} - f_i^{an}|}{|f_i^{an}|} \qquad (2.15)$$

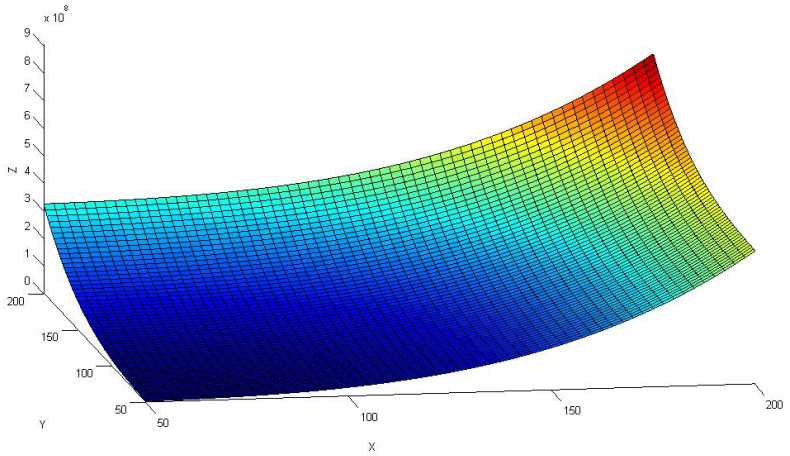

Figure 2.1: Topography given by the expression 2.14 over the grid $x = y = [50 : 200]$ spaced in both direction by $2.5\,m$.

Analytic and discrete values have been estimated on a regular grid of testing points belonging to the surface 2.14 with $x = y = [60 : 160]$ spaced in both directions by $5\,m$.To compute the discrte derivatives the incremental values h and k have been taken both equal to $2.5\,m$. In figure $2.2 - 2.6$ the derivatives f_x, f_y, f_{xx}, f_{yy} and f_{xy} are plotted in the order. The results show errors ranging between $0.02 - 0.17\%$ for the first-order derivatives, and between $0.005 - 0.03\%$ for the second-order derivatives. Notice that the mixed derivative is constant, and the error is actually zero. Notice further that the largest error values for f_x, f_{xx} and for f_y, f_{yy} are reached expectedly for the minimum values of the variables x and y.

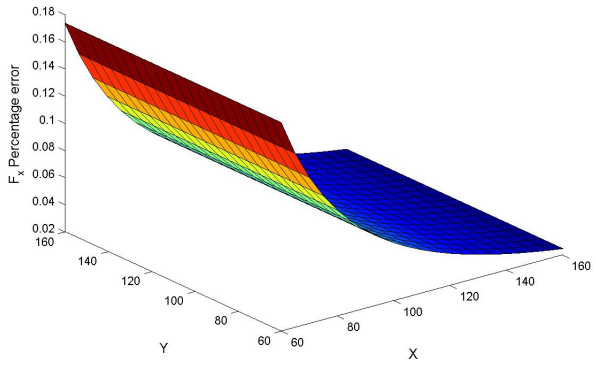

Figure 2.2: Percentage discretization error of f_x.

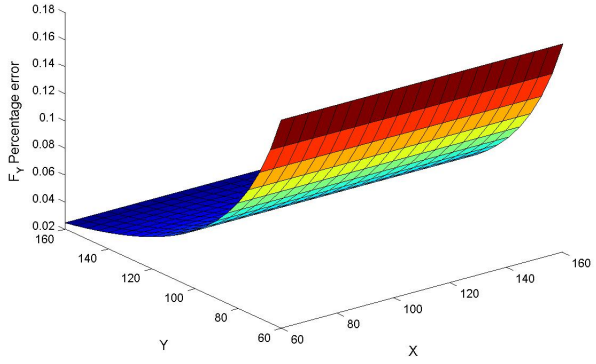

Figure 2.3: Percentage discretization error of f_y.

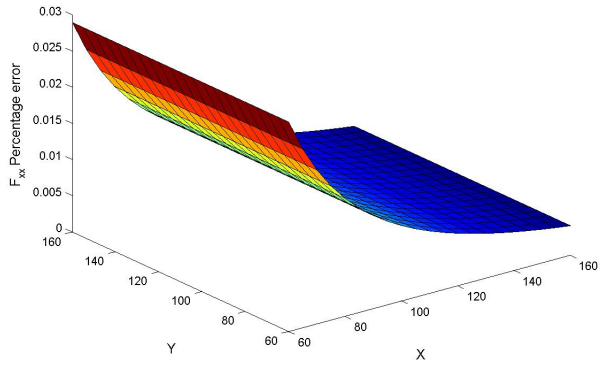

Figure 2.4: Percentage discretization error of f_{xx}.

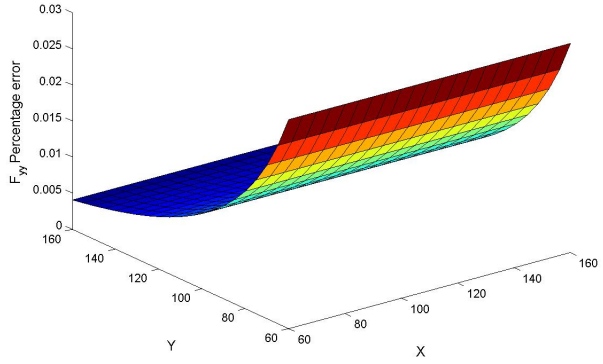

Figure 2.5: Percentage discretization error of f_{yy}.

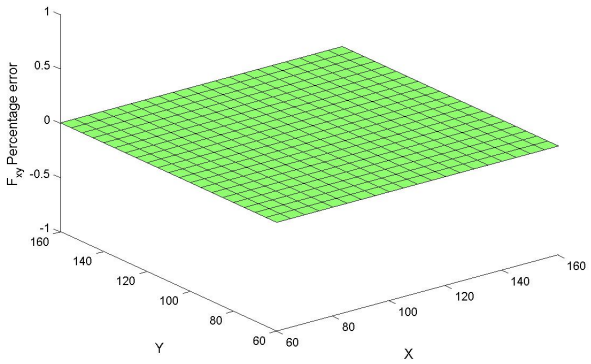

Figure 2.6: Percentage discretization error of f_{xy}.

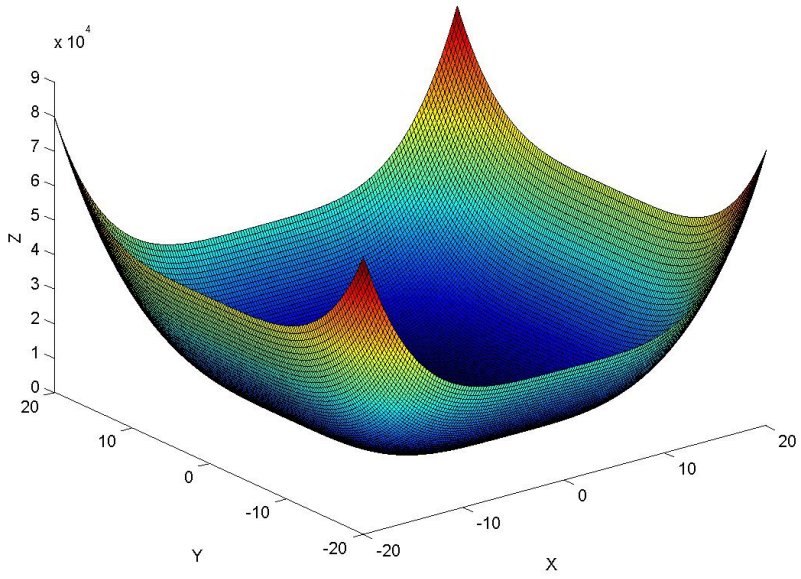

Figure 2.7: Topography given by the function 2.14 represented in the range $x = y = [-20 : +20]$ spaced in both direction by $0.25\,m$.

.

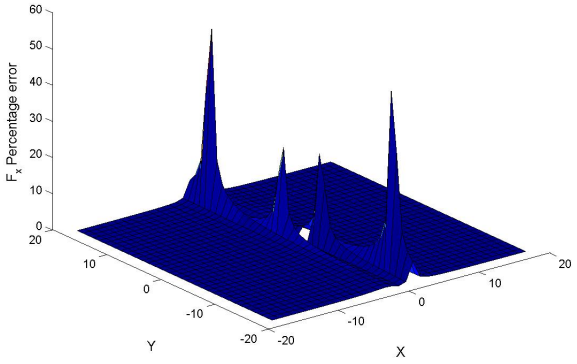

Figure 2.8: Percentage discretization error of f_x. Notice the spikes that are located close to the points where the analytical derivative vanishes.

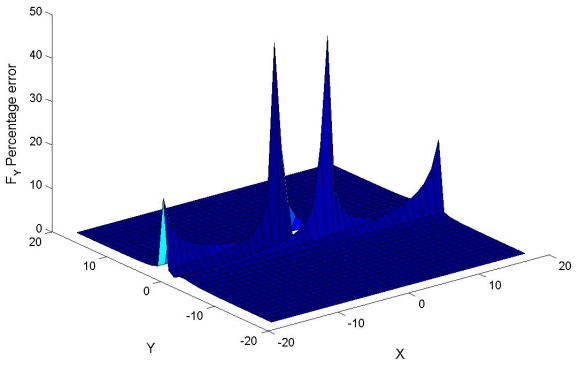

Figure 2.9: Percentage discretization error of f_y. Notice the spikes that are located close to the points where the analytical derivative vanishes.

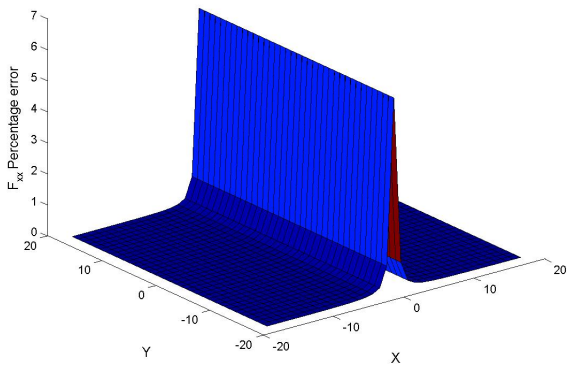

Figure 2.10: Percentage discretization error of f_{xx}. Notice that the error diverges as x^{-2} as x approaches 0.

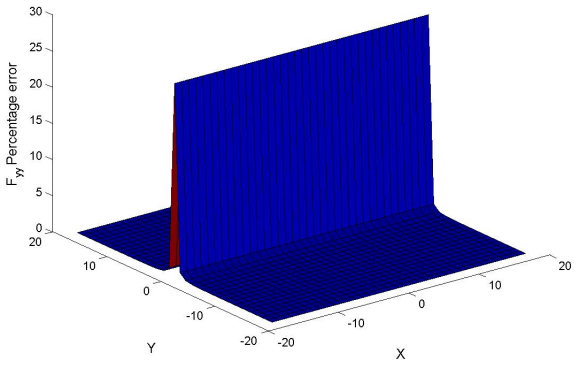

Figure 2.11: Percentage discretization error of f_{yy}. Notice that the error diverges as y^{-2} as y approaches 0.

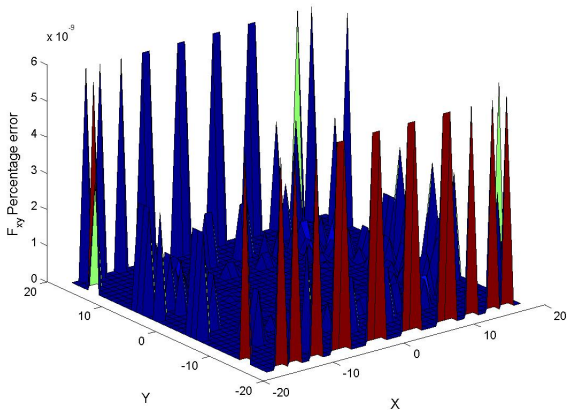

Figure 2.12: Percentage discretization error of f_{xy}. In this case the discetisation formula is exact and discrepancies are random and only due to numerical rounding errors.

Around the points where the analytical derivatives vanish, the percentage error is expected to grow infinite according to the inverse of the square of the distance. To test this behavior, we have explored the derivatives in proximity to the origin where the analytical derivatives of the studied topography go to zero. The explored region is the grid $x = y = [-20 : +20]$ spaced in both directions by $0.25\,m$ and is plotted in (figure 2.7). The grid with the test points is in the interval $x = y = [-16 : +16]$ spaced in both directions by $0.5\,m$. The incremental step for the computations of all derivatives are $h = k = 0.25\,m$. As we can see from the results $2.8 - 2.12$ the errors output shows several spikes in the first-order derivatives and a regular growth in the second-order derivatives f_{xx} and f_{yy}. Indeed the behavior is the same, that is a percentage error growth of the type d^{-2} when the distance from the test point to the point where the analytical derivatives vanish goes to zero. This is more evident where the vanishing curve is well captured by the test grid nodes (like in the plots of f_{xx} and f_{yy}) and less evident when such curves pass through the nodes at different distances and the resulting spikes seem randomly distributed. Local maximum of $40 - 50\%$ can be seen in the first-order derivatives, while in the second-order ones we find 7% maximum for f_{xx} and 20% for f_{yy}. On the contrary, mixed derivatives errors are very close to 0 since the formulas provide exact results for the chosen function: the discrepancy is quite small and only due to numerical rounding errors.

As we will see in the next chapters, computing the motion of a point or more points on a surface requires the computation of quantities involving the surface and its derivatives up to the second-order along the trajectories of the moving

points at each time step. Since the positions of the points might be arbitrary and in general do not coincide with the nodes of a discrete grid, there is the need to compute all the required functions by means of opportune methods of interpolation. Let us assume that one needs to compute the variable g in the position $P = (x, y)$ that happens to belong to the grid cell delimited by the four grid nodes (x_i, y_j), (x_i, y_{j+1}), (x_{i+1}, y_{j+1}) and (x_{i+1}, y_j). We have tested two interpolation methods on the polynomial function 2.14 and on all its relevant derivatives. The first one is an inverse-distance interpolation.

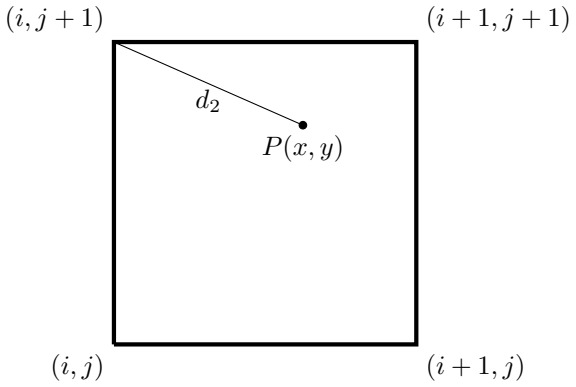

Figure 2.13: Inverse-distance interpolation. Only the distance d_2 of the point P to the vertex 2 is shown.

The interpolation formula is a weighted average where the weights are the inverse of the geometrical distances of the point $P(x, y)$ to the vertices of the cell, that is:

$$g = \frac{g_1/d_1 + g_2/d_2 + g_3/d_3 + g_4/d_4}{1/d_1 + 1/d_2 + 1/d_3 + 1/d_4}$$

where the indexes $1 - 4$ represent the cell vertices, from the node i, j going clockwise .
In order to assess the effect of the interpolation on the computation of the discrete derivatives, we have used the values of the discrete derivatives coalculated on the grids introduced in the previous examples 2.1 and 2.7, and then we have built two additional test grids, actually staggered, and in these nodes we have calculated the derivatives through interpolation. . The two tested grids, one in the larger domain and the other in the smaller domain around the origin, are formed resepctively by nodes $x = y = [60 : 4.3 : 160]$ and by nodes $x = y = [-16 : 0.85 : +16]$. The interpolated functions have been then compared to the corresponding analytical values. The resulting percentage errors are shown in the following figures:

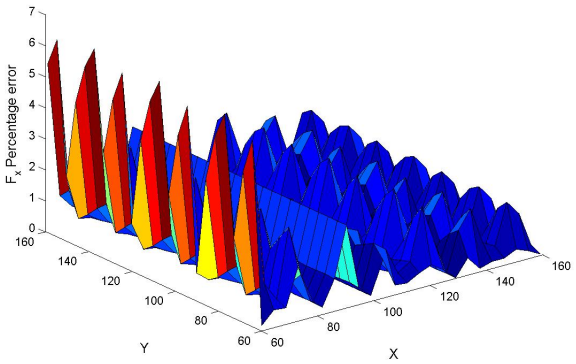

Figure 2.14: Percentage error of f_x evaluated on points over the staggered test grid. Inverse-distance interpolation.

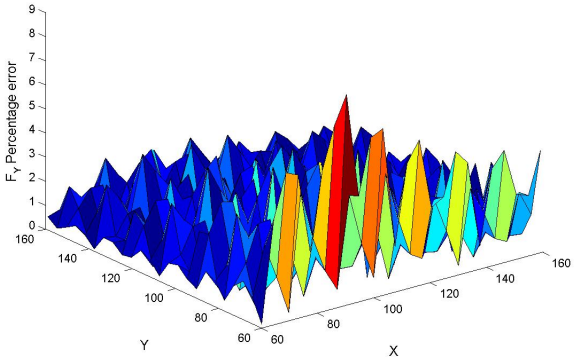

Figure 2.15: Percentage error of f_y evaluated on points over the staggered test grid. Inverse-distance interpolation.

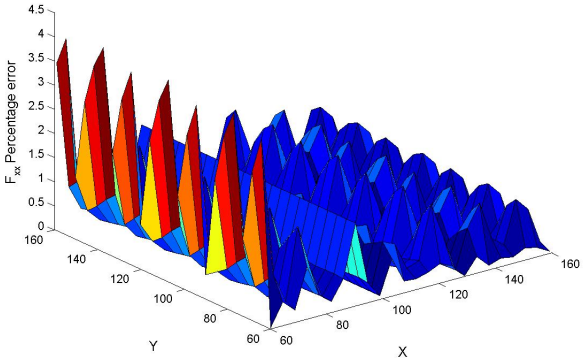

Figure 2.16: Percentage error of f_{xx} evaluated on points over the staggered test grid. Inverse-distance interpolation.

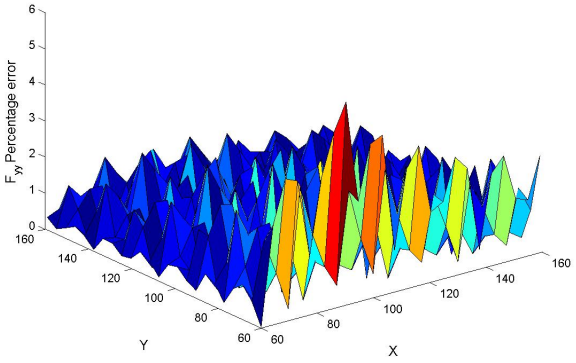

Figure 2.17: Percentage error of f_{yy} evaluated on points over the staggered test grid. Inverse-distance interpolation.

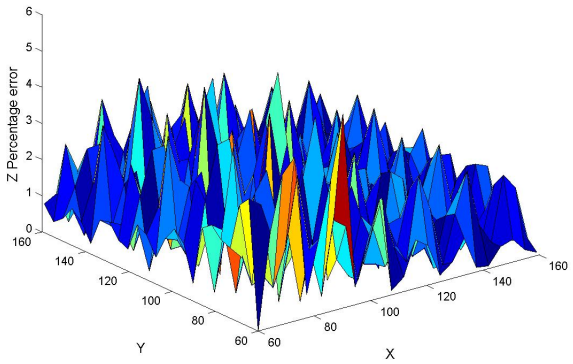

Figure 2.18: Percentage error of z evaluated on points over the staggered test grid. Inverse-distance interpolation.

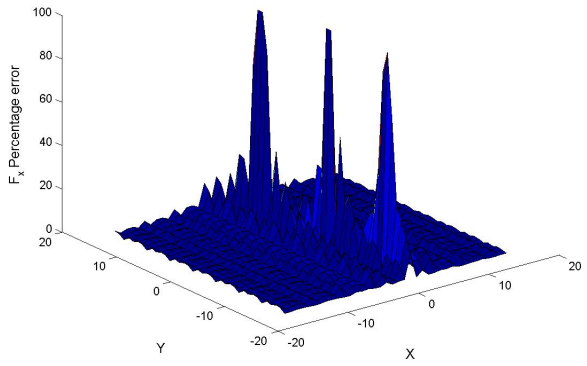

Figure 2.19: Percentage error of f_x evaluated on points over the staggered test grid around the origin. Inverse-distance interpolation.

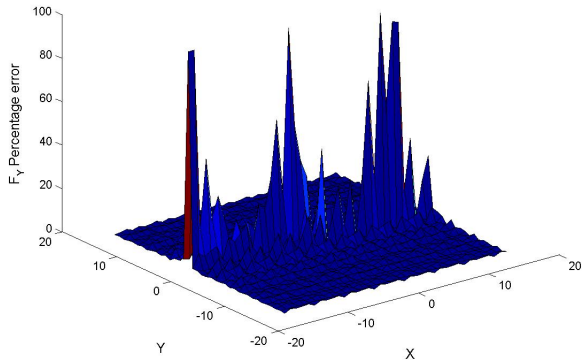

Figure 2.20: Percentage error of f_y evaluated on points over the staggered test grid around the origin. Inverse-distance interpolation.

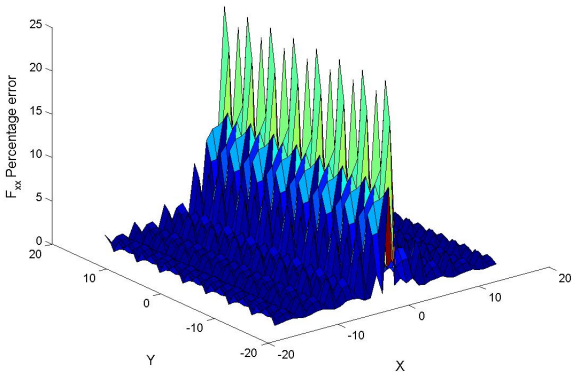

Figure 2.21: Percentage error of f_{xx} evaluated on points over the staggered test grid around the origin. Inverse-distance interpolation.

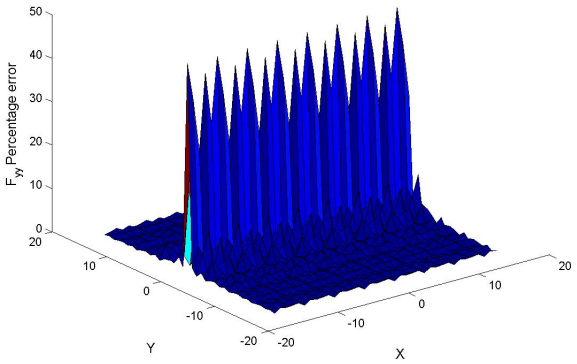

Figure 2.22: Percentage error of f_{yy} evaluated on points over the staggered test grid around the origin. Inverse-distance interpolation.

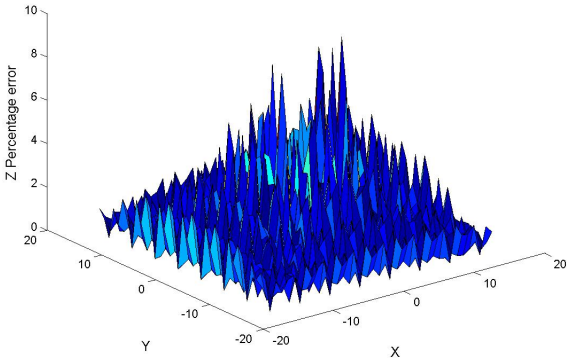

Figure 2.23: Percentage error of z evaluated on points over the staggered test grid around the origin. Inverse-distance interpolation.

Errors values for the first grid reach the maximum of 6% for the first-order derivatives and of3.5% for the second-order ones and for the topography function $z = f$. This suggests us that in general this interpolation method could lead even to bigger errors on irregular geometries. In fact, as we can see from the last set of figures ($2.19 - 2.23$), the errors near origin, that for the derivatives of this function is a critical region $(x = 0, y = 0)$, become large reaching local values of 100% in f_x, 80% for f_y, 25% for f_{xx}, 40% for f_{yy} and 8% for the

function z.
This interpolation study conducted on the polynomial function has been extended also on many other functions with more complex shapes. The results happened to be even worse in some cases. Hence, we have explored a different kind of interpolation process, that uses more than a single cell. In particular, the best results have been obtained by a *bicubic interpolation* (spline) method. Basically, this is an extension of a cubic interpolation technique to interpolate data sets on a two dimensional regular grid. In the application to the case of the fourth-degree polynomial, it is found that the interpolation errors are not larger than the discretization errors. We show here below the results of the interpolation test only for the staggered grid around the origin previously introduced.

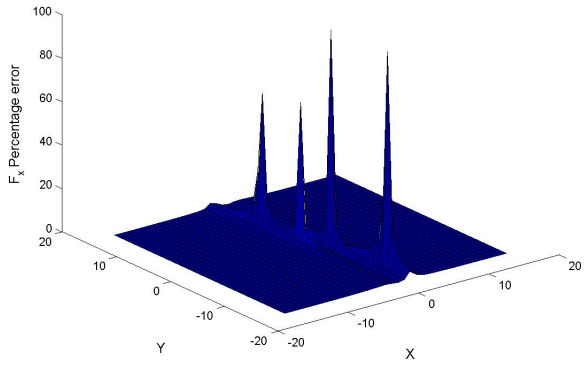

Figure 2.24: Percentage error of f_x evaluated on points over the staggered test grid around the origin. Bicubic spline interpolation.

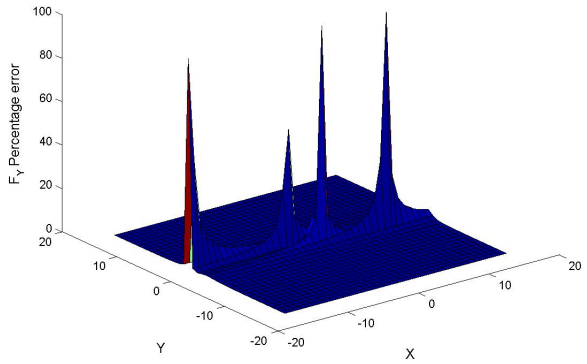

Figure 2.25: Percentage error of f_y evaluated on points over the staggered test grid around the origin. Bicubic spline interpolation.

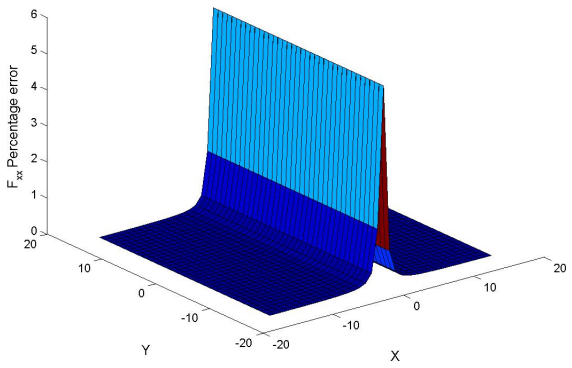

Figure 2.26: Percentage error of f_{xx} evaluated on points over the staggered test grid around the origin. Bicubic spline interpolation.

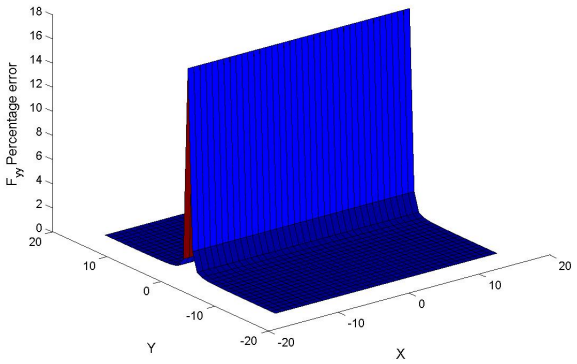

Figure 2.27: Percentage error of f_{yy} evaluated on points over the staggered test grid around the origin. Bicubic spline interpolation.

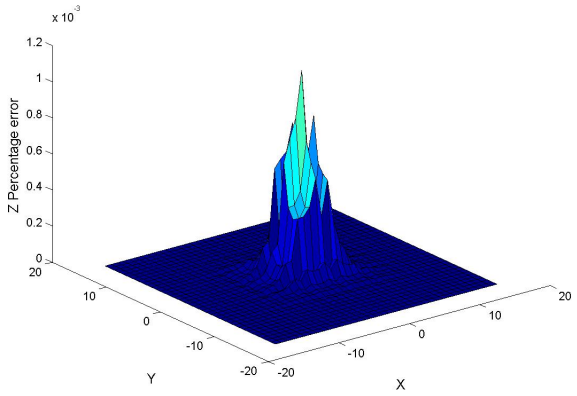

Figure 2.28: Percentage error of z evaluated on points over the staggered test grid around the origin. Bicubic spline interpolation.

The results (figure 2.24 − 2.28) show clearly the good performance of the spline interpolation process. In particular, for the topography function$z$ we have maximum errors of $10^{-3}\%$ against the $8 - 9\,\%$ of the inverse-distance-based interpolation technique. For second-order derivatives we have much better results than in previous test. Still, we have isolated peaks in the first-order derivatives but, as we have seen, this is due to the discretization itself and not to the interpolation.

Chapter 3

Dynamics of a point sliding on a surface

3.1 1D Equations of motion

In this chapter we outline the basic mathematics of the motion of a point mass sliding on a surface. We start from the simplest case of a 1D problem to gain a better understanding of the physical background, and therefore we assume that the motion occurs in the plane (y, z) and that the point-particle moves on the curve $z = f(y)$:

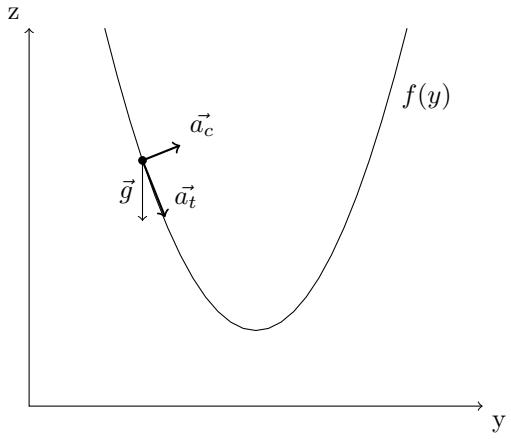

Figure 3.1: Point acceleration components and gravitational acceleration ($\vec{g}$). $\vec{a_c}$ and $\vec{a_t}$ are the centripetal and tangential components.

On the trajectory curve, the driving force being the gravity, the motion is

described by means of the tangential (a_t) and centripetal (a_c) accelerations:

$$\vec{a} = \vec{a_t} + \vec{a_c}$$

Splitting $\vec{a}$ into the Cartesian components:

$$\begin{cases} \vec{a_y} = \vec{a_{ty}} + \vec{a_{cy}} \\ \vec{a_z} = \vec{a_{tz}} + \vec{a_{cz}} \end{cases}$$

and considering that a_t is due to the contribution of the gravity acceleration along the sliding curve, we can write:

$$a_t = g_{eff} = g \sin\theta$$

where θ is the local angle of slope, that is the angle between the slope and the horizontal y axis. Taking this into account, the y and z components of $\vec{a_t}$ result to be:

$$\begin{cases} a_{ty} = g \sin\alpha \cos\theta \\ a_{tz} = -g \sin^2\alpha \end{cases}$$

Remebering that $a_c = v^2/R$, where v is the point velocity and R is the local radius of curvature, we can write:

$$\begin{cases} a_{cy} = \frac{-v^2}{R} \sin\theta \\ \\ a_{cz} = \frac{v^2}{R} \cos\theta \end{cases}$$

Summing up, if we use the dot notation to designate time derivatives, we obtain:

$$\begin{cases} \dot{v_y} = g \sin\theta \cos\theta - \frac{v^2}{R} \sin\theta \\ \\ \dot{v_z} = -g \sin\sin^2\theta + \frac{v^2}{R} \cos\theta \end{cases}$$

where the velocity square modulus is obviously given by $v^2 = v_y^2 + v_z^2$. Since the point is constrained to move on the surface, then its vertical position z is linked to y through the relation $z = f(y)$, and so:

$$\begin{cases} v_y = \dot{y} = v \cos\theta \\ v_z = \dot{z} = \dot{y} f'(y) = v_y f'(y) \end{cases}$$

Re-writing all the equations in function of y, we obtain:

$$\dot{y} = v_y \tag{3.1}$$

$$\dot{v_y} = -g \sin\theta \cos\theta - \frac{v_y^2 + v_z^2}{R} \sin\theta \tag{3.2}$$

$$\dot{z} = v_z \tag{3.3}$$

$$\dot{v_y} = -g \sin^2\theta + \frac{v_y^2 + v_z^2}{R} \cos\theta \tag{3.4}$$

Through simple differential geometry considerations it is possible to express the angle $\theta(y)$ by means of the first derivative of the function $f(y)$:

$$f'(y) = \tan\theta \;\Rightarrow\; \theta = \arctan f'(y)$$

and hence to obtain the following relations:

$$\cos\theta = \frac{1}{\sqrt{1+\tan^2\theta}} = \frac{1}{\sqrt{1+f'(y)^2}}$$
$$\sin\theta = \frac{\tan\theta}{\sqrt{1+\tan^2\theta}} = \frac{f'(y)}{\sqrt{1+f'(y)^2}}$$

Also the radius of curvature can be written as a function of the first and second order derivatives of $f(y)$:

$$R = \frac{(1+f'(y)^2)^{3/2}}{f''(y)}$$

Thus, the general expression for the equations describing the particle motion are:

$$\dot{y} = v_y \tag{3.5}$$
$$\dot{v_y} = -g\frac{f'(y)}{1+f'(y)^2} - v_y^2\frac{f'(y)}{1+f'(y)^2}f''(y) \tag{3.6}$$
$$\dot{z} = v_y f'(y) \tag{3.7}$$
$$\dot{v_z} = -g\frac{f'(y)^2}{1+f'(y)^2} - v_y^2\frac{1}{1+f'(y)^2}f''(y) \tag{3.8}$$

As it is clear from 3.5-3.8 we just have two independent equations. Indeed the last two equations of the above system do not need to be solved. Once the horizontal position y of the particle is known, the vertical position is also known being $z = f(y)$. The last two equations express the vertical velocity and acceleration of the particles in terms of its horizontal counterparts. For this reason this is a one dimensional problem, even if the motion actually develops over a $2D$ curve.

3.2 2D Equations of motion

We now find the equations describing the motion of a particle moving on a surface described by the analytic functon $z = f(x, y)$. Hence, we need to solve a 2D problem, since the vertical position of the particle is simply evaluated from its horizontal coordinates $x$and y.
Let us consider the surface function and the generic tangent vector over it:

$$z = f(x, y) \Rightarrow z - f(x, y) = 0$$

$$\vec{t} = \begin{vmatrix} a \\ b \\ af_x + bf_y \end{vmatrix}$$

where a and b are arbitrary coefficients. The normal vector is defined by $\vec{t} \cdot \vec{n} = 0$, so:

$$\begin{vmatrix} a \\ b \\ af_x + bf_y \end{vmatrix} \cdot \begin{vmatrix} x \\ y \\ z \end{vmatrix} = 0$$

$$\downarrow$$

$$\begin{aligned} ax + by + z(af_x + bf_y) = 0 \\ a(x + zf_x) + b(y + zf_y) = 0 \end{aligned} \tag{3.9}$$

Setting $z = 1$, we obtain $n_x = -f_x$ and $n_y = -f_y$.So the normal $\vec{n}$ can be written as:

$$\vec{n} = \begin{vmatrix} -f_x \\ -f_y \\ 1 \end{vmatrix}$$

and the unit normal vector is:

$$\hat{n} = \frac{\vec{n}}{||n||} = \begin{vmatrix} -f_x \\ -f_y \\ 1 \end{vmatrix} \frac{1}{(f_x^2 + f_y^2 + 1)^{1/2}}$$

We need the maximum steepness vector $\vec{s}$ (and the corresponding unit vector $\hat{s}$) that is the tangential vector that is obtained by projecting $\hat{n}$ over the tangential plane, and results to be:

$$\vec{s} = \begin{vmatrix} -f_x \\ -f_y \\ -f_x^2 - f_y^2 \end{vmatrix} \rightarrow \hat{s} = [f_x^2 + f_y^2 + (f_x^2 + f_y^2)^{1/2}]^{-1/2} \cdot \vec{s}$$

The point acceleration can be written as:

$$a = a_t \cdot \hat{s} + a_n \cdot \hat{n} \tag{3.10}$$

in terms of the tangential and normal components a_t and a_n respectively. Taking the gravity acceleration as $\vec{g} = (0, 0, -g)$, the tangential acceleration takes the form:

$$\begin{aligned} a_t = \vec{g} \cdot \hat{s} &= \frac{g(f_x^2 + f_y^2)}{f_x^2 + f_y^2 + (f_x^2 + f_y^2)^2} \begin{vmatrix} -f_x \\ -f_y \\ -f_x^2 - f_y^2 \end{vmatrix} \\ &= \frac{g}{1 + f_x^2 + f_y^2} \begin{vmatrix} -f_x \\ -f_y \\ -f_x^2 - f_y^2 \end{vmatrix} \end{aligned}$$

For the normal component, we get:

$$a_n = \vec{a} \cdot \hat{n} = \frac{d}{dt}\vec{v} \cdot \hat{n} =$$

$$= -\vec{v} \cdot \frac{d\hat{n}}{dt} = -\vec{v} \cdot \left[(\frac{d\vec{x}}{dt}) \cdot (\frac{d\hat{n}}{dx}) \right] = \vec{v} \cdot (\vec{v} \cdot \nabla \hat{n})$$

After some manipulations, the above expression becomes:

$$a_n = \frac{v_x^2 f_{xx} + v_x v_y f_{xy} + v_y^2 f_{yy}}{\sqrt{1 + f_x^2 + f_y^2}}$$

Eventually, the equations describing this kind of motion are:

$$\dot{x} = v_x \tag{3.11}$$

$$\dot{v_x} = -g \frac{f_x}{1 + f_x^2 + f_y^2} - \left(v_x^2 f_{xx} + v_x v_y f_{xy} + v_y^2 f_{yy} \right) \frac{f_x}{1 + f_x^2 + f_y^2} \tag{3.12}$$

$$\dot{y} = v_y \tag{3.13}$$

$$\dot{v_y} = -g \frac{f_y}{1 + f_x^2 + f_y^2} - \left(v_x^2 f_{xx} + v_x v_y f_{xy} + v_y^2 f_{yy} \right) \frac{f_y}{1 + f_x^2 + f_y^2} \tag{3.14}$$

As already remarked before, the vertical position of the particle can be derived from the horizontal coordinates x and y and vertical velocity and acceleration are correspondingly given by:

$$\dot{z} = v_z = f_x v_x + f_y v_y.$$

$$\dot{v_z} = f_x \dot{v_x} + f_y \dot{v_y} + v_x (f_{xx} v_x + f_{xy} v_y) + v_y (f_{yx} v_x + f_{yy} v_y) =$$

$$= f_x \dot{v_x} + f_y \dot{v_y} + f_{xx} v_x^2 + f_{yy} v_y^2 + v_x v_y f_{xy}$$

Substituting 3.12 and 3.14 in the previous equation we find:

$$\dot{v_z} = -g \frac{f_x^2 + f_y^2}{1 + f_x^2 + f_y^2} + \left(v_x^2 f_{xx} + v_x v_y f_{xy} + v_y^2 f_{yy} \right) \frac{1}{1 + f_x^2 + f_y^2} \tag{3.15}$$

3.2.1 Friction

To introduce the resistant acceleration due to friction forces, we have to add to 3.10 the appropriate term, which is opposite to the velocity direction:

$$\vec{a} = a_t \cdot \hat{s} + a_n \cdot \hat{n} + \mu (g_n - a_n) \hat{v} \tag{3.16}$$

where μ is the friction coefficient depending on the material properties of the moving particle and of the sliding surface. Here g_n is the component of the

gravity acceleration in the normal direction and $\hat{v}$ is the unit vector parallel to the velocity, i.e.:

$$g_n = \vec{g} \cdot \vec{n} = \frac{-g}{\sqrt{1 + f_x^2 + f_y^2}} \tag{3.17}$$

$$\hat{v} = \frac{1}{\sqrt{v_x^2 + v_y^2 + v_z^2}} \begin{vmatrix} v_x \\ v_y \\ v_z \end{vmatrix}$$

$$= \frac{1}{\sqrt{v_x^2 + v_y^2 + (v_x f_x + v_y f_y)^2}} \begin{vmatrix} v_x \\ v_y \\ v_x f_x + v_y f_y \end{vmatrix}$$

If we incorporate the last equations in the 3.11-3.14 we find the final equations of motion:

$$\dot{x} = v_x \tag{3.18}$$

$$\dot{v_x} = -g\frac{f_x}{1 + f_x^2 + f_y^2} - \gamma_{xy}\frac{f_x}{1 + f_x^2 + f_y^2} + \mu\Gamma_{xy}\frac{v_x}{\sqrt{v_x^2 + v_y^2 + (v_x f_x + v_y f_y)^2}} \tag{3.19}$$

$$\dot{y} = v_y \tag{3.20}$$

$$\dot{v_y} = -g\frac{f_y}{1 + f_x^2 + f_y^2} - \gamma_{xy}\frac{f_y}{1 + f_x^2 + f_y^2} + \mu\Gamma_{xy}\frac{v_y}{\sqrt{v_x^2 + v_y^2 + (v_x f_x + v_y f_y)^2}} \tag{3.21}$$

Where:

$$\Gamma_{xy} = \frac{-g}{\sqrt{1 + f_x^2 + f_y^2}} - \frac{v_x^2 f_{xx} + v_x v_y f_{xy} + v_y^2 f_{yy}}{\sqrt{1 + f_x^2 + f_y^2}}$$

The vertical velocity and accelerations can be computed from the horizontal quantities through the same procedure seen in the case with no friction.

3.3 Main Runge-Kutta discretization Method

To solve the equations 3.18–3.21 we used an explicit Runge-Kutta at fourth order. The matrix of the a_i coefficients is:

$$A = \begin{vmatrix} 0 & 0 & 0 & 0 \\ 0.5 & 0 & 0 & 0 \\ 0 & 0.5 & 0 & 0 \\ 0 & 0 & 1 & 0 \end{vmatrix}$$

The coefficients for the temporal partition are:

$$c_1 = 0 \qquad c_2 = 1/2 \qquad c_3 = 1/2 \qquad c_4 = 1$$

while the coefficients for the computation of the next step quantities are:

$$\beta_1 = 1/6 \qquad \beta_2 = 1/3 \qquad \beta_3 = 1/3 \qquad \beta_4 = 1/6$$

Setting the initial position and velocity of the particle at the values they have at the previous time step k, we can evaluate the solution using the same procedure seen in chapter 2. In this case in the first sub-step we have:

$$\begin{aligned} w_{1x} &= x_0 \\ w_{1y} &= y_0 \\ w_{1vx} &= vx_0 \\ w_{1vy} &= vy_0 \\ \tilde{f_{1x}} &= \dot{x}_0 = vx_0 \\ \tilde{f_{1y}} &= \dot{y}_0 = vy_0 \\ \tilde{f_{1vx}} &= \dot{v}_{x0} \\ \tilde{f_{1vy}} &= \dot{v}_{y0} \end{aligned}$$

For the second sub-step we have:

$$\begin{aligned} w_{2x} &= x_0 + k/2\tilde{f_{1x}} \\ w_{2y} &= y_0 + k/2\tilde{f_{1y}} \\ w_{2vx} &= vx_0 + k/2\tilde{f}_{1vx} \\ w_{2vy} &= vy_0 + k/2\tilde{f}_{1vy} \\ \tilde{f_{2x}} &= w_{2vx} \\ \tilde{f_{2y}} &= w_{2vy} \\ \tilde{f}_{2vx} &= \dot{w}_{2vx} \\ \tilde{f}_{2vy} &= \dot{w}_{2vy} \end{aligned}$$

In the third one:

$$\begin{aligned} w_{3x} &= x_0 + k/2\tilde{f_{2x}} \\ w_{3y} &= y_0 + k/2\tilde{f_{2y}} \\ w_{3vx} &= vx_0 + k/2\tilde{f}_{2vx} \\ w_{3vy} &= vy_0 + k/2\tilde{f}_{2vy} \\ \tilde{f_{3x}} &= w_{3vx} \\ \tilde{f_{3y}} &= w_{3vy} \\ \tilde{f}_{3vx} &= \dot{w}_{3vx} \\ \tilde{f}_{3vy} &= \dot{w}_{3vy} \end{aligned}$$

and in the last sub-step we have:

$$
\begin{aligned}
w_{4x} &= x_0 + k\tilde{f_{3x}} \\
w_{4y} &= y_0 + k\tilde{f_{3y}} \\
w_{4vx} &= vx_0 + k\tilde{f}_{3vx} \\
w_{4vy} &= vy_0 + k\tilde{f}_{3vy} \\
\tilde{f_{4x}} &= w_{4vx} \\
\tilde{f_{4y}} &= w_{4vy} \\
\tilde{f}_{4vx} &= \dot{w}_{4vx} \\
\tilde{f}_{4vy} &= \dot{w}_{4vy}
\end{aligned}
$$

When we write $\dot{w}_{iv}x$ or $\dot{w}_{iv}y$ we mean the acceleration of the mass evaluated in the previous sub-step (for $i = 2, 3, 4$) or at the previous time step (for $i = 0$). The explicit expression for this value depends on the forces we consider. For example, if we consider just the gravity acting on the surface, we use 3.11 and 3.14. As a matter of fact, the procedure structure is always in this form. Even when we will handle the case of more interacting particles, the solution will be provided in the same way. Basically, we just need to change the expressions for the acceleration case by case.
At every time step, the solution for the particle is estimated by:

$$x_{RK} = x_{k+1} = x_k + \Delta t\,(1/6\tilde{f}_{1x} + 1/3\tilde{f}_{2x} + 1/3\tilde{f}_{3x} + 1/6\tilde{f}_{4x})$$

$$y_{RK} = y_{k+1} = y_k + \Delta t\,(1/6\tilde{f}_{1y} + 1/3\tilde{f}_{2y} + 1/3\tilde{f}_{3y} + 1/6\tilde{f}_{4y})$$

$$v_{xRK} = v_{x\,k+1} = v_{xk} + \Delta t\,(1/6\tilde{f}_{1vx} + 1/3\tilde{f}_{2vx} + 1/3\tilde{f}_{3vx} + 1/6\tilde{f}_{4vx})$$

$$v_{yRK} = v_{y\,k+1} = v_{y\,k} + \Delta t\,(1/6\tilde{f}_{1vy} + 1/3\tilde{f}_{2vy} + 1/3\tilde{f}_{3vy} + 1/6\tilde{f}_{4vy})$$

where Δt is the time step.

3.4 Applications to ideal no-friction topographies

As was underlined in the previous sections, no general solution to the problem of a particle moving on a surface exists. The previous analysis, however, provides a system of ODEs governing the dynamics of the particle over the analytic surface $z = f(x, y)$ and we can call the numerical solution to this system a semi-analytical solution. Using a MATLAB code, we have solved the equations of motion through the fourth-order Runga-Kutta method described in section 3.3 (in short an RK4 method) obtaining a description of particle motion that is very accurate. Comparison with merely analytical solutions available in cases of plane surfaces shows that the RK4 solutions are practically undistinguishable from the analaytical ones within the range of times and velocities of geophysical interests.
The main goal of having a solution built in this way, is that we can compare it with solutions obtained by means of numerical models when even analytical surfaces are discretized. In the following we perform such a comparison by

solving the same cases by means of the RK4 method and by a means of a 2D block model developed by the Tsunami Research Team of the Department of Physics and Astronomy (DIFA) of the University of Bologna and widey applied to compute the dynamics of subaerial and submarine landslides (see [*Tinti et al.*] 2000;*Tinti et al.*, 2003; *Tinti et al.*, 2004]). The code, called UBO-BLOCK2, describes a slide as a matrix of blocks with a quadrilateral base able to interact while sliding down over a slope and adopts a Lagrangian point of view. The sliding surface is discretised in triangles. In the first stage of discretization, the slide is partitioned into the constituent blocks that can be equalized either in the base or in the volume. During the motion, they can change their shape keeping their volume constant, although, interpenetration of blocks is not allowed. Basically, the motion is characterized at every time step by geometrical and kinematic properties of each block. The model UBO-BLOCK2 is written in FORTRAN77 programming language.
In the following examples, we solve the problem described by the 3.11-3.14 and when using the RK4 method we compute all the derivatives analytically. When using the model UBO-BLOCK2, the friction forces are disabled, and, since we assume that the landslide is formed only by one block, interaction forces do not play any role. We further note that we take a unitary mass that starts from a rest state with initial zero velocity.

3.4.1 Parabolic topography

The first bottom surface we propose for the comparison of the models is described by a simple parabolic function, that is:

$$f(x,y) = ax^2 + by^2 + dx + f; \tag{3.22}$$

where the values of the coefficients are:

$$a = 0.00005 \quad b = 0.01 \quad d = -0.1 \quad f = 50$$

The first- and second-order derivatives are:

$$\frac{\partial f}{\partial x} = 2ax + d \quad \frac{\partial f}{\partial y} = 2by$$

$$\frac{\partial f^2}{\partial x^2} = 2a \quad \frac{\partial f^2}{\partial y^2} = 2b \quad \frac{\partial f^2}{\partial x \partial y} = 0$$

The grid to represent the surface is built in the intervals $x = [0 : 1000]\, m$ and $y = [-100 : 100]\, m$ with equal space steps $dx = dy = 1m$. In the MATlLAB routine the time array is $t = [0 : 60]\, s$, while in the UBO-BLOCK2 model it stops at $t = 50s$. In both simulations the time step is $dt = 0.5\, s$. The starting position is in $(x = 10, y = -90)\, m$. In the F77 programme a single block cube with a $2\, m$ side is defined as the landslide body.

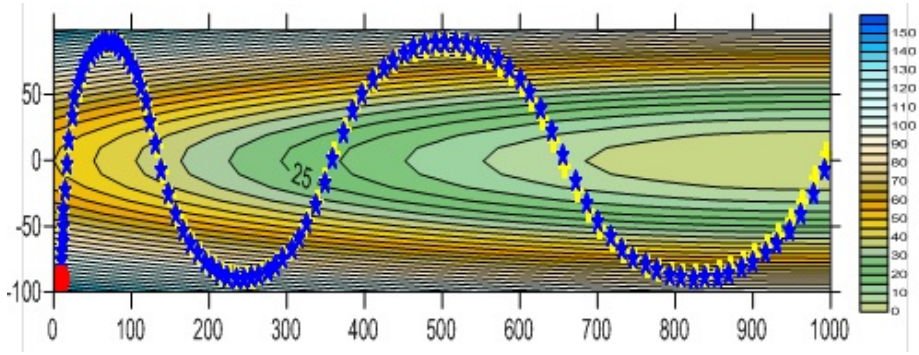

Figure 3.2: Comparison between trajectories from analytical (MATLAB RK4, blue) and numerical (UBO-BLOCK2, yellow) simulation. The initial landslide roof is shown in red. The bottom surface is represented by a contour map. The elevation scale is shown on the right.

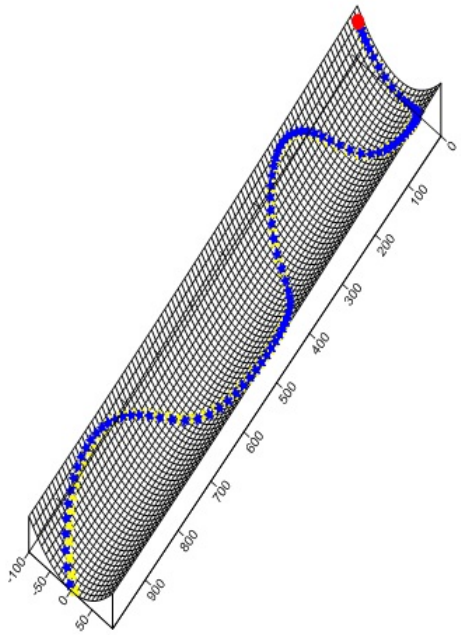

Figure 3.3: Same results shown in figure 3.2 but with a 3D view perspective.

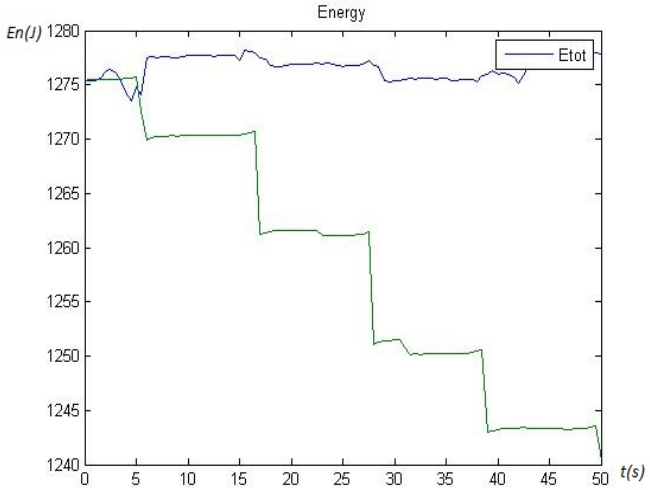

Figure 3.4: Total (potential + kinetic) energy trends: analytic (blue), numerical (green).

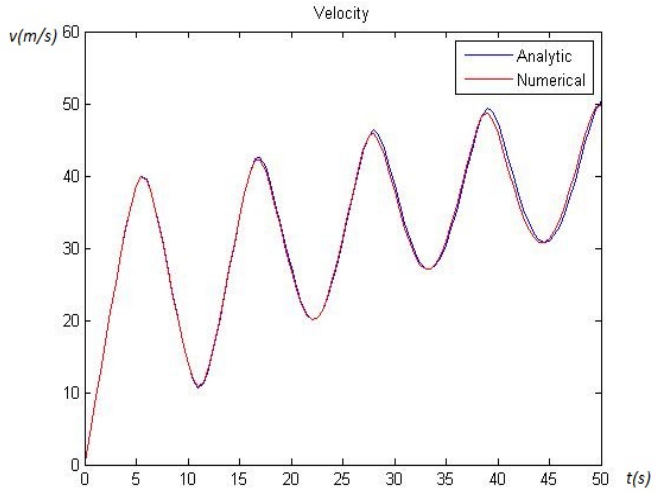

Figure 3.5: Velocity trends: analytic (blue), numerical (red).

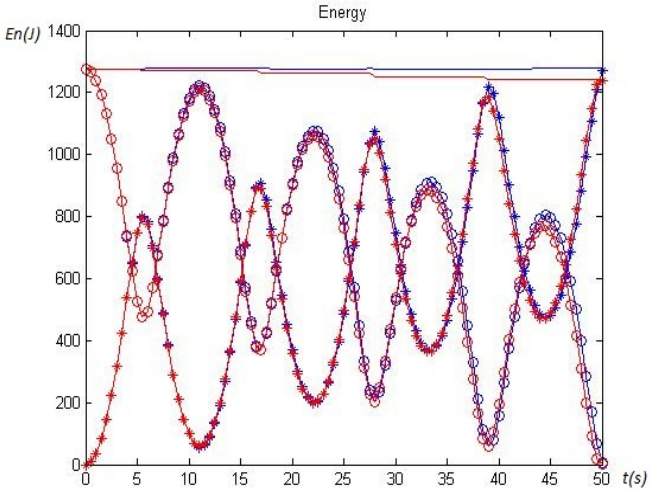

Figure 3.6: Total energy (solid line) and energy components: kinetic (asterisks), potential (open circles). Analytical solution (blue) vs. numerical (red).

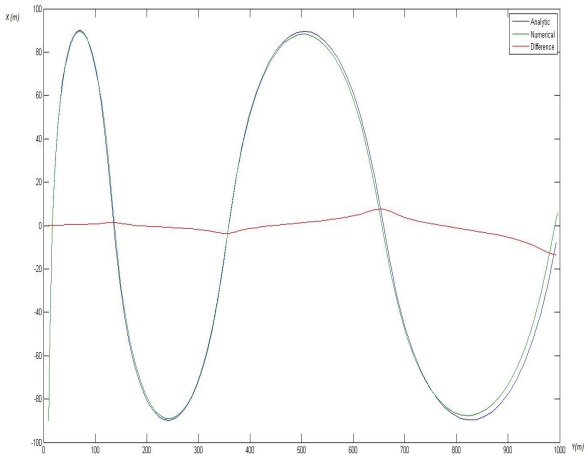

Figure 3.7: Particle trajectories in the horizontal plane: analytical (blue) and numerical (green). The absolute difference is also shown in red.

The results of the simulation are shown in figures 3.2- 3.7. From figures 3.2 , 3.3 and 3.5 it is clear that trajectories and velocities are quite similar. To allow a better trajectory comparison, a planar view from above is shown in figure 3.7

together with the x-distance between them.
Some discrepancy is evident in the energy result (figures 3.4 and 3.6) with the UBO-BLOCK2 model exhibiting some energy dissipation. When the trajectory has a big change in direction, the energy loss is small. Instead energy loss is higher in correspondence with velocity peaks , i.e. when the point is in the trough and the velocity is higher, corresponding to a change of sign in the acceleration. This could suggest a problem in the numerical routine, possibly related to the way UBO-BLOCK2 evaluates the acceleration (second order derivative) of the 'next step'.

3.4.2 Gaussian topography

The second surface considered is given by a Gaussian function:

$$f(x,y) = e^{-(x^2/2b^2+y^2/2c^2)}$$

Where $b = c = 30$.The first- and second-order derivatives are:

$$\frac{\partial f}{\partial x} = -\frac{x}{b^2} * f(x,y) \quad ; \quad \frac{\partial f}{\partial y} = -\frac{y}{c^2} * f(x,y)$$

$$\frac{\partial f^2}{\partial x^2} = -\frac{1}{b^2} * f(x,y) * (1 - \frac{x^2}{b^2})$$
$$\frac{\partial f^2}{\partial y^2} = -\frac{1}{c^2} * f(x,y) * (1 - \frac{y^2}{c^2})$$
$$\frac{\partial f^2}{\partial y \partial x} = f(x,y) * \frac{xy}{c^2 b^2};$$

In this case the grid is represented by two row vectors $x = y = [-100 : 1 : 100]\, m$. The simulation time step is $dt = 0.2\, s$ for the MATLAB code and $dt = 0.5\, s$ for the F77 code. The initial position of the particle is set on $(x = 5,\, y = 5)\, m$. As in the previous case, the UBO-BLOCK2 landslide is formed by one $2\, m$-side cube centered in $(5, 5)\, m$.

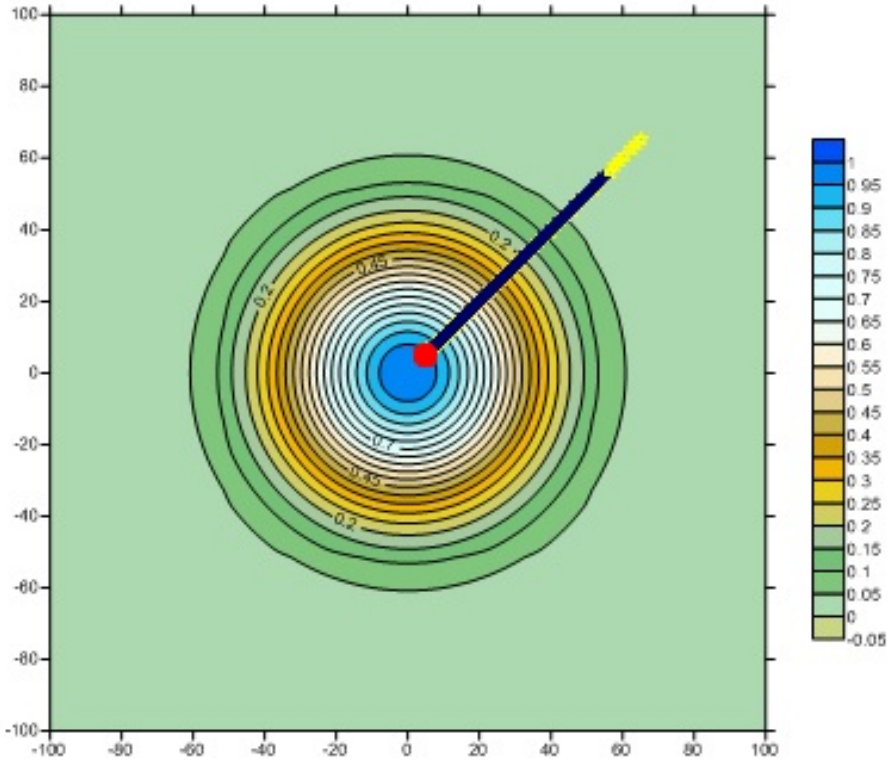

Figure 3.8: Comparison between trajectories from analytical (MATLAB RK4, blue) and numerical (UBO-BLOCK2, yellow) simulation. The initial landslide roof is shown in red. The bottom surface is represented by a contour map. The elevation scale is shown on the right.

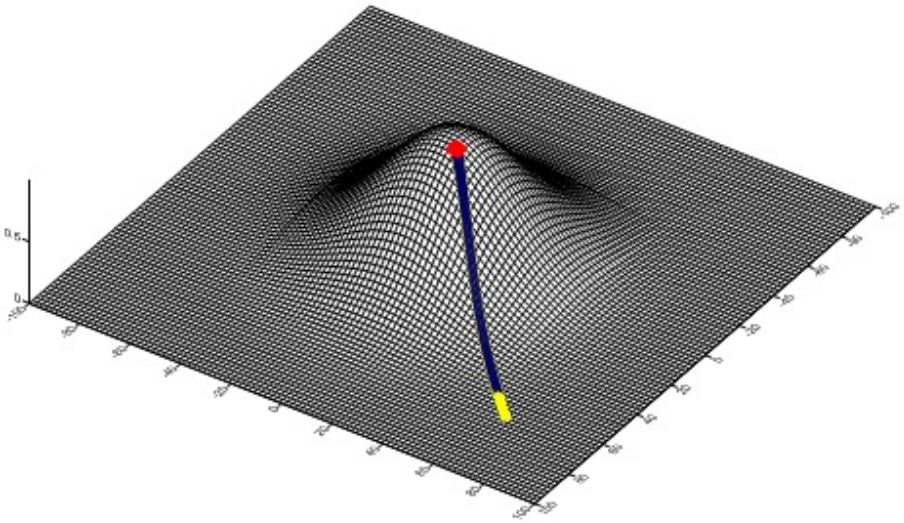

Figure 3.9: Same results shown in figure 3.8 but with a 3D view perspective.

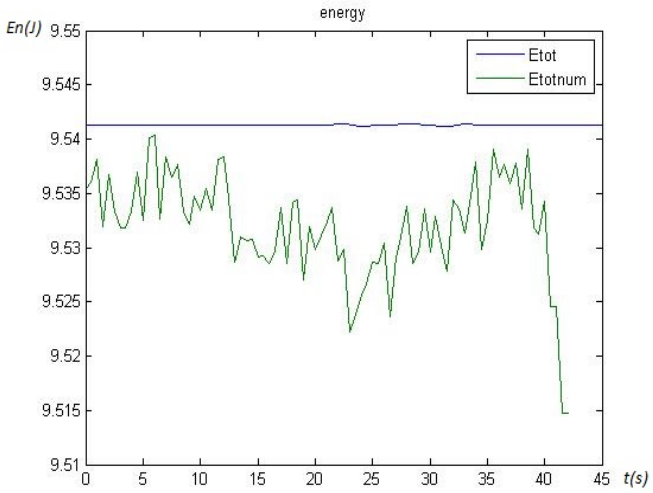

Figure 3.10: Total (potential + kinetic) energy trends: analytical (blue), numerical (green).

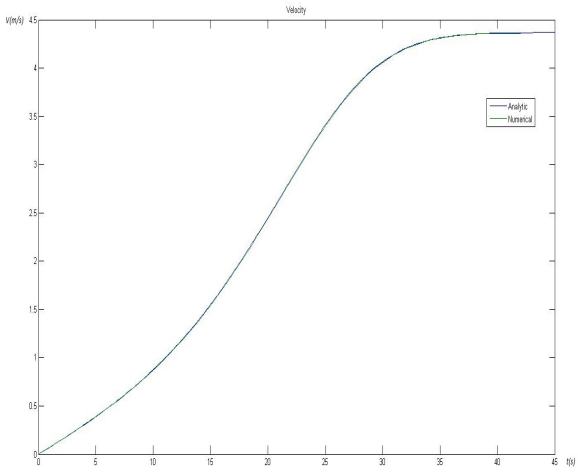

Figure 3.11: Velocity trends: analytic (blue), numerical (green).

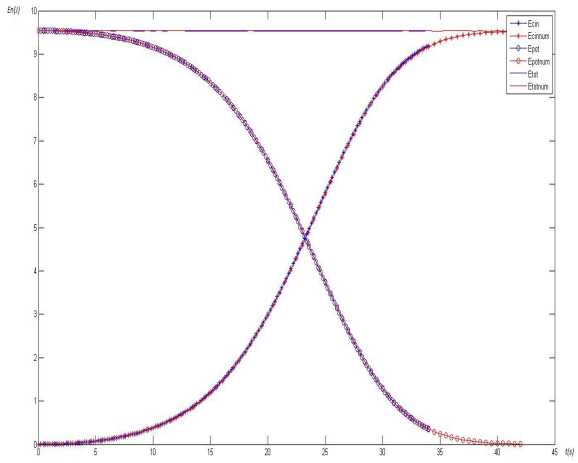

Figure 3.12: Total energy (solid line) and energy components: kinetic (asterisks), potential (open circles). Analytical solution (blue) vs. numerical (red).

The simulation results are shown in figures 3.8– 3.12.

The paths match perfectly (figures 3.8– 3.9). Energy is almost constant: the discrepancy among the two simulations is less then 1% (figure 3.10). The velocities are almost overlapped (Figure 3.11). The particle has its maximum

speed at the end of the slope; extending the time range, the velocity become constant (as it should be because the friction is zero). There is also a perfect balance between potential and kinetic energies (figure 3.12).

3.4.3 Multiple-ridge topography

The functions used in the previous cases can be taken as representative of a valley or of a single mountain block. To test the codes in a more complex situation, we have chosen a topography showing a sequence of crest and valleys like in the radial direction, i.e. :

$$f(x,y) = \frac{\sin(r)}{r} \qquad r = \sqrt{a(x^2+y^2)}$$

Where $a = 0.05$. The first-and second-order derivatives are:

$$\frac{\partial f}{\partial x} = \frac{xcos(r)}{x^2+y^2} - \frac{xa\sin(r)}{r^3}$$

$$\frac{\partial f}{\partial y} = \frac{ycos(r)}{x^2+y^2} - \frac{ya\sin(r)}{r^3}$$

$$\frac{\partial f^2}{\partial x^2} = \frac{\cos(r)}{x^2+y^2} - \frac{3x^2\cos(r)}{(x^2+y^2)^2} - \frac{a\sin(r)}{r^3} + \frac{3a^2x^2\sin(r)}{r^5} - \frac{x^2a^2\sin(r)}{r^3}$$

$$\frac{\partial f^2}{\partial y^2} = \frac{\cos(r)}{x^2+y^2} - \frac{3y^2\cos(r)}{(x^2+y^2)^2} - \frac{a\sin(r)}{r^3} + \frac{3a^2y^2\sin(r)}{r^5} - \frac{y^2a^2\sin(r)}{r^3}$$

$$\frac{\partial f^2}{\partial x \partial y} = -\frac{axy\sin(r)}{r(x^2+y^2)} - \frac{3xy\cos(r)}{(x^2+y^2)^2} + \frac{3a^2xy\sin(r)}{r^5}$$

Space and time arrays are the same as in the previous simulation. The initial position of the particle is $(1,1)$, and on this point is centered the cubic landslide of $2\,m$ thickness handled by UBO-BLOCK2.

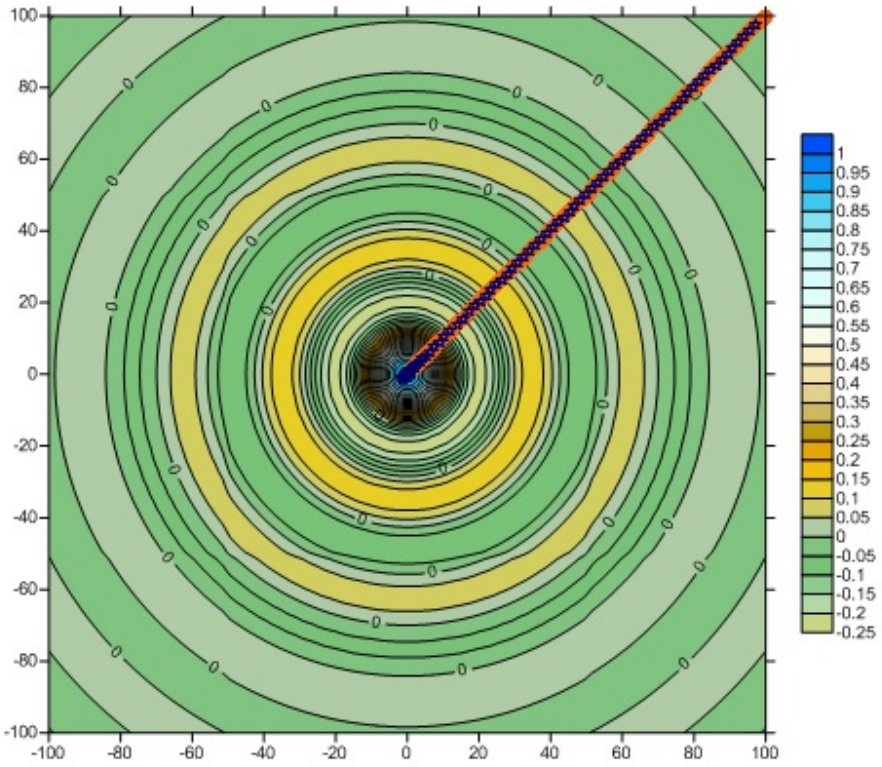

Figure 3.13: Comparison between trajectories from analytical (MATLAB RK4, blue) and numerical (UBO-BLOCK2, yellow) simulation. The initial landslide roof is shown in red. The bottom surface is represented by a contour map. The elevation scale is shown on the right.

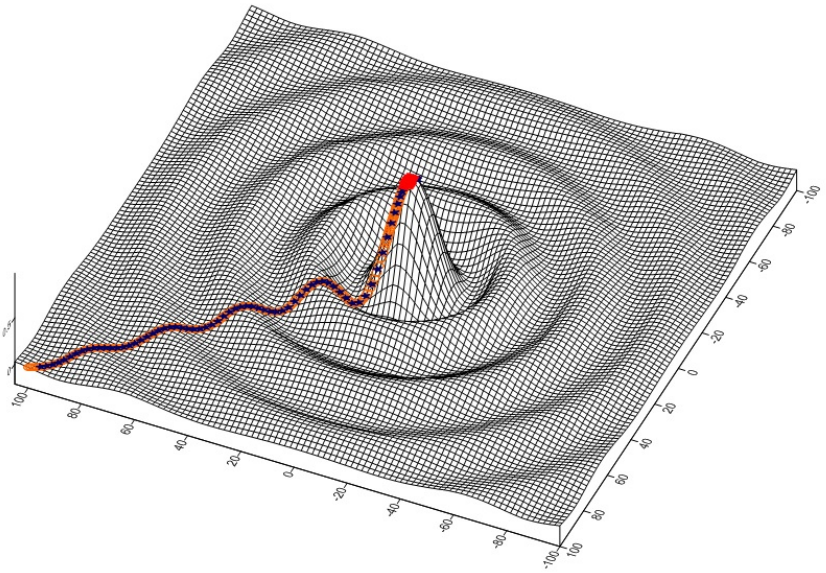

Figure 3.14: Same results shown in the previous figure 3.13, but with a 3D view perspective.

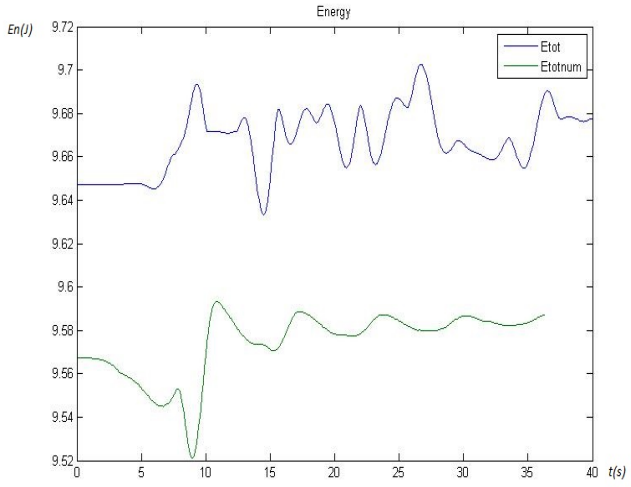

Figure 3.15: Total (potential + kinetic) energy trends: analytical (blue), numerical (green).

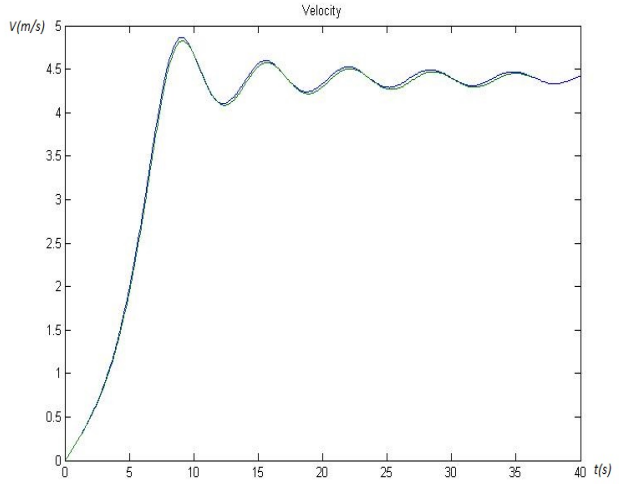

Figure 3.16: Velocity trends: analytic (blue), numerical (green).

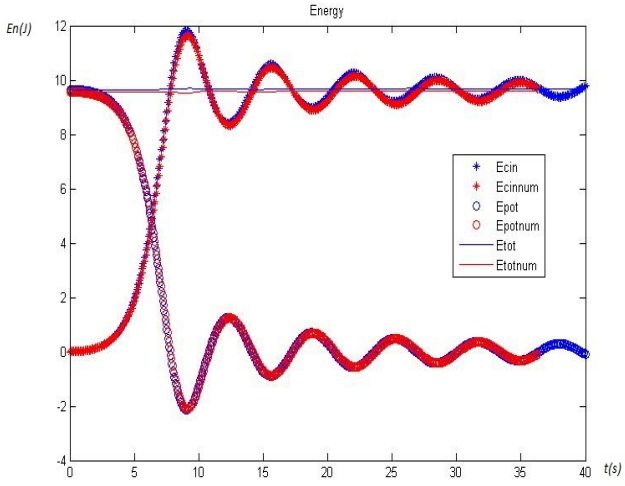

Figure 3.17: Total energy (solid line) and energy components: kinetic (asterisks), potential (open circles). Analytical solution (blue) vs. numerical (red).

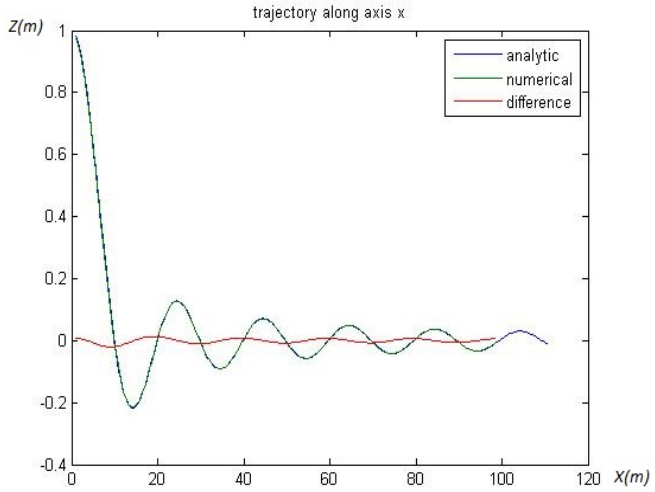

Figure 3.18: Trajectory along x axis: analytic (blue) and numerical (green). The difference is shown in red.

The results are shown in figures 3.13– 3.17. There is a very good match between the trajectories (figures 3.13– 3.14) and their x-distance is quite small (figure 3.18), being almost constant proving the similarity. The velocity trends shows a good match too (figure 3.16). The difference among the energy trends does not exceed 1% (figure 3.15). An expansion of the energy components is shown in figure 3.17. As it should be, kinetic energy maxima correspond with potential energy minima, and viceversa.

3.4.4 Topography with a linear, exponentially damped, trend

The last example we treat is a topography that alternates a mountain with a deep depression around the origin, that is:

$$f(x,y) = xe^{-a(x^2+y^2)}$$

Where $a = 0.001$. Writing $\psi = e^{-a(x^2+y^2)}$, the first- and second-order derivatives are:

$$\frac{\partial f}{\partial x} = \psi(1-2ax^2) \quad \frac{\partial f}{\partial y} = -\psi 2axy$$

$$\frac{\partial^2 f}{\partial x^2} = \psi 2ax(2ax^2-3) \quad \frac{\partial^2 f}{\partial y^2} = \psi 2ax(2ay^2-1)$$

$$\frac{\partial^2}{\partial x \partial y} = \psi 2ay(2ax^2-1)$$

Space and time arrays for the MATLAB simulation are $x = [-900 : 1 : 100]\, m$, $y = [-100 : 1 : 100]\, m$ and $t = [0 : 0.5 : 20]\, s$. The initial position is in the point $(50, 10)$. The $2\, m$ square-base landslide has a $2m$ thickness.

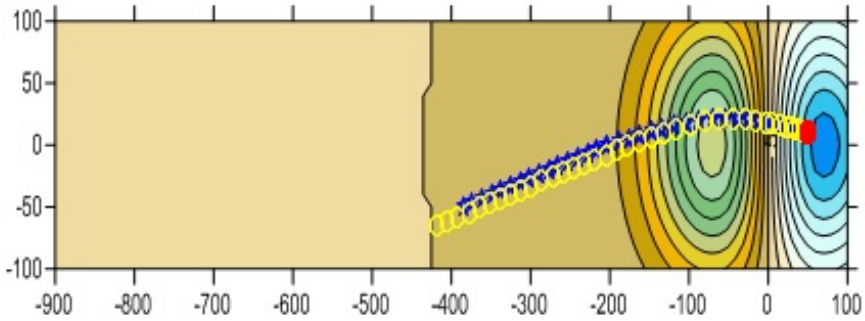

Figure 3.19: Comparison between trajectories from analytical (MATLAB RK4, blue) and numerical (UBO-BLOCK2, yellow) simulation. The initial landslide roof is shown in red. The bottom surface is represented by a contour map. The elevation scale is shown on the right.

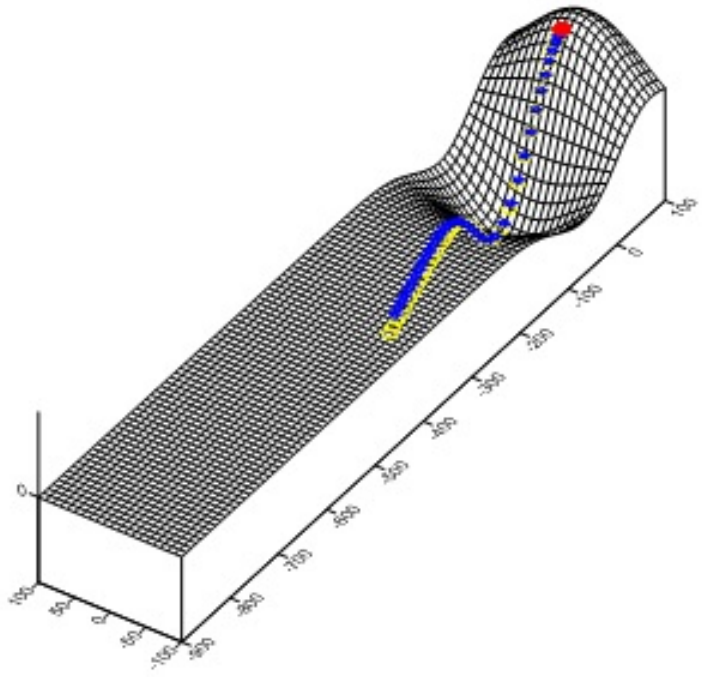

Figure 3.20: Same results shown in figure 3.19, but with a 3D view perspective.

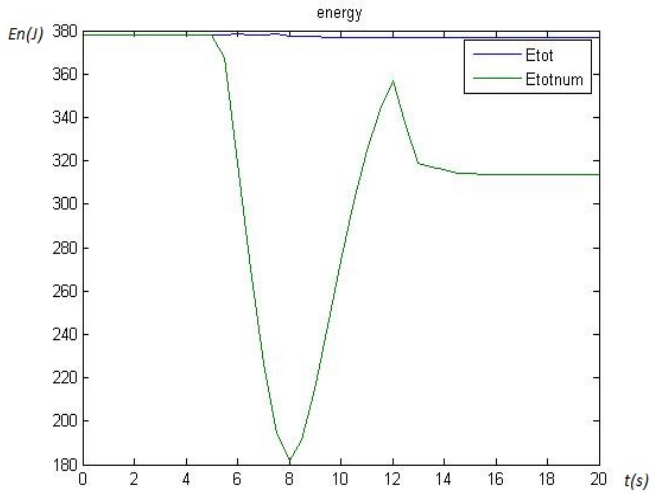

Figure 3.21: Total (potential + kinetic) energy trends: analytical (blue), numerical (green).

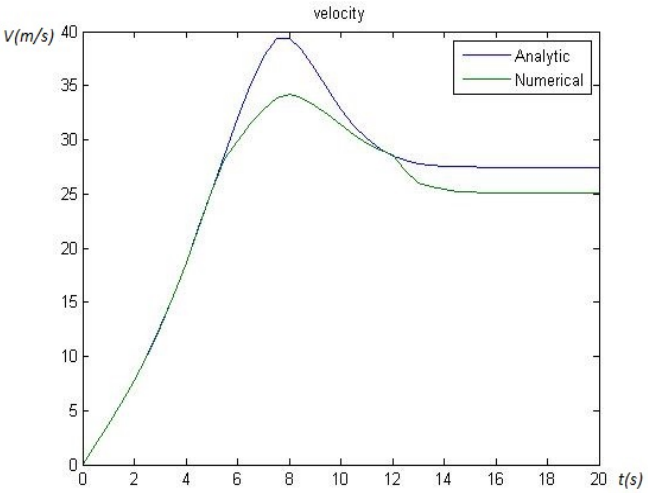

Figure 3.22: Velocity trends: analytic (blue), numerical (green).

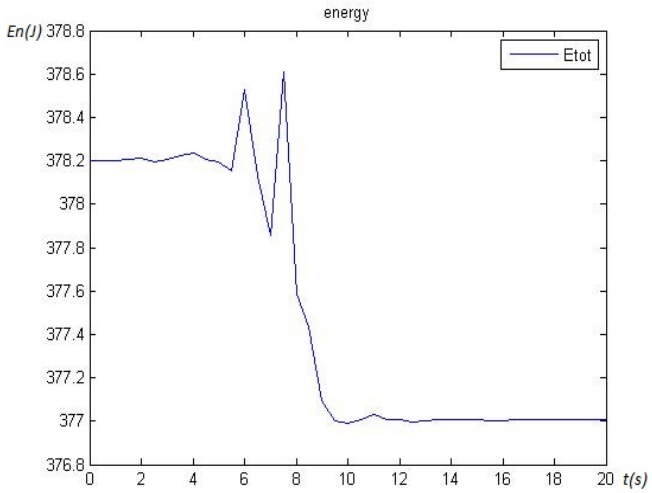

Figure 3.23: Energy trend from Analytic simulation.

The results are shown in figures 3.19−3.23. The two trajectories have some differences after the second considerable change of slope. The same differences can be found in the velocity trend (figure 3.22): the numerical F77 simulation provides a smaller velocity maximum. The largest simulation discrepancies are in the energy trends. As it is clear in figure 3.21, there is a big energy collapse in the F77 results linked to the first change in slope. The MATLAB solution energy (figure 3.23) is instead constant (apart from a small perturbation around 0.3%). This example shows that the F77 code needs improvements facing local strong high-gradient slopes of the provided sliding surface.

Chapter 4

Dynamics of points sliding on a surface and interacting

4.1 Interaction force among two material points

We want to describe the motion of particles sliding on a surface and interacting. We illustrate here below the theory for two interacting particles, with the interaction being such that the 3D Cartesian distance between the particles is constant: this is a good approximation for rocks, since, even though they can deform during motion, displacements are always quite small with respect to the typical dimension of the body. We suppose the sliding surface is described by the function $z = f(\vec{x})$, where $\vec{x} = (x, y)$. The particles have coordinates $\vec{r}_1$ and $\vec{r}_2$ in the space. So, we have $\vec{x}_1$ and $\vec{x}_2$ in the Cartesian plane and z_1 and z_2 in the vertical direction. Hence, we can write the position points as:

$$P_1 = (\vec{x}_1, f(\vec{x}_1)) \qquad P_2 = (\vec{x}_2, f(\vec{x}_2))$$

The distance between the particles can be written as:

$$d_{12} = (\vec{r_1} - \vec{r_2}) \circ (\vec{r_1} - \vec{r_2}) = (\vec{x}_1 - \vec{x}_2) \circ (\vec{x}_1 - \vec{x}_2) + (z_1 - z_2)^2$$

where $\circ$ denotes the dot product. The equations of motion are:

$$\begin{cases} m_1 \ddot{\vec{x}}_1 = \vec{F}_1 + \vec{h}_{12} \\ m_2 \ddot{\vec{x}}_2 = \vec{F}_2 - \vec{h}_{21} \end{cases} \tag{4.1}$$

where $\vec{F}_1$ and $\vec{F}_2$ are the forces acting on the points (gravity, friction and reaction force) and $\vec{h}_{12}$ is the interaction force. We suppose that $\vec{h}_{12}$ is the force acting on P_1 by P_2 and $\vec{h}_{21} = -\vec{h}_{12}$ is the one acting on P_2 by P_1.

Extracting the acceleration from 4.1, we obtain:

$$\begin{cases} \ddot{\vec{x}}_1 = (\vec{F}_1 + \vec{h}_{12}) \frac{1}{m_1} \\ \ddot{\vec{x}}_2 = (\vec{F}_2 - \vec{h}_{12}) \frac{1}{m_2} \end{cases}$$

Subtracting the previous equation:

$$\ddot{\vec{x}}_1 - \ddot{\vec{x}}_2 = \frac{\vec{F}_1}{m_1} - \frac{\vec{F}_2}{m_2} + \frac{\vec{h}_{12}}{m_1} + \frac{\vec{h}_{12}}{m_2} = \frac{\vec{F}_1}{m_1} - \frac{\vec{F}_2}{m_2} + \frac{m_1 + m_2}{m_1 m_2} \vec{h}_{12}$$

We can use the invariance of d_{12} to obtain $(\ddot{\vec{x}}_1 - \ddot{\vec{x}}_2)$. Deriving two times d_{12}^2 with respect to time:

$$2(\dot{\vec{x}}_1 - \dot{\vec{x}}_2) \circ (\vec{x}_1 - \vec{x}_2) + 2(\dot{z_1} - \dot{z_2}) = 0$$

$$\downarrow$$

$$(\ddot{\vec{x}}_1 - \ddot{\vec{x}}_2) \circ (\vec{x}_1 - \vec{x}_2) + (\dot{\vec{x}}_1 - \dot{\vec{x}}_2 \circ)(\dot{\vec{x}}_1 - \dot{\vec{x}}_2) + (\ddot{z}_1 - \ddot{z}_2)(z_1 - z_2) + (\dot{z}_1 - \dot{z}_2) = 0$$

The difference among the accelerations is given by the 4.1. Replacing it in the previous equation we obtain :

$$\frac{m_1 + m_2}{m_1 m_2} \vec{h}_{12} \circ (\vec{x}_1 - \vec{x}_2) =$$

$$(\vec{x}_1 - \vec{x}_2) \circ (\frac{\vec{F}_1}{m_1} - \frac{\vec{F}_2}{m_2}) - (\dot{x}_1 - \dot{x}_2) \circ (\dot{x}_1 - \dot{x}_2) - (\ddot{z}_1 - \ddot{z}_2)(z_1 - z_2) - (\dot{z}_1 - \dot{z}_2)^2$$

The previous relation shows how the invariance of the distance between the particles implies that the interaction force in the direction of the line joining the two points on the Cartesian plane is determined. We now assume that $\vec{h}_{12}$ lies on the $(\vec{r}_1 - \vec{r}_2)$ direction, that is:

$$\vec{h}_{12} = h_{12} \frac{\vec{r}_1 - \vec{r}_2}{[(\vec{r}_1 - \vec{r}_2) \circ (\vec{r}_1 - \vec{r}_2)]^{1/2}} \tag{4.2}$$

$$\downarrow$$

$$\frac{m_1 + m_2}{m_1 m_2} \vec{h}_{12} \circ (\vec{x}_1 - \vec{x}_2) = \frac{m_1 + m_2}{m_1 m_2} h_{12} \frac{(\vec{x}_1 - \vec{x}_2) \circ (\vec{x}_1 - \vec{x}_2)}{[(\vec{r}_1 - \vec{r}_2) \circ (\vec{r}_1 - \vec{r}_2)]^{1/2}}$$

Hence, the modulus of h_{12} is given in the form:

$$h_{12} = -\frac{m_1 m_2}{m_1 + m_2} \frac{[(\vec{r}_1 - \vec{r}_2) \circ (\vec{r}_1 - \vec{r}_2)]^{1/2}}{(\vec{x}_1 - \vec{x}_2) \circ (\vec{x}_1 - \vec{x}_2)} \times$$

$$[(\vec{x}_1 - \vec{x}_2) \circ (\frac{\vec{F}_1}{m_1} - \frac{\vec{F}_2}{m_2}) + (\dot{x}_1 - \dot{x}_2) \circ (\dot{x}_1 - \dot{x}_2) + (\ddot{z}_1 - \ddot{z}_2)(z_1 - z_2) + (\dot{z}_1 - \dot{z}_2)^2]$$

Using 4.2 we can write the expression of $\vec{h}_{12}$:

$$\vec{h}_{12} = -\frac{m_1 m_2}{m_1 + m_2} \frac{[(\vec{r}_1 - \vec{r}_2)}{(\vec{x}_1 - \vec{x}_2) \circ (\vec{x}_1 - \vec{x}_2)} \times \tag{4.3}$$

$$[(\vec{x}_1 - \vec{x}_2) \circ (\frac{\vec{F}_1}{m_1} - \frac{\vec{F}_2}{m_2}) + (\dot{x}_1 - \dot{x}_2) \circ (\dot{x}_1 - \dot{x}_2) + (\ddot{z}_1 - \ddot{z}_2)(z_1 - z_2) + (\dot{z}_1 - \dot{z}_2)^2]$$

If we switch the indexes in the previous relation we can find $\vec{h}_{21}$ and we can verify that:

$$\vec{h}_{21} = -\vec{h}_{12}$$

For the general form, we can use the indexes i, j:

$$\vec{h}_{ij} = -\frac{m_i m_j}{m_i + m_j} \frac{[(\vec{r}_i - \vec{r}_j)}{(\vec{x}_i - \vec{x}_j) \circ (\vec{x}_i - \vec{x}_j)} (\alpha_{ij} + \beta_{ij}) \tag{4.4}$$

Where:

$$\alpha_{ij} = (\vec{x}_i - \vec{x}_j) \circ (\frac{\vec{F}_i}{m_i} - \frac{\vec{F}_j}{m_j}) + (\dot{x}_i - \dot{x}_j) \circ (\dot{x}_i - \dot{x}_j) + (\dot{z}_i - \dot{z}_j)^2$$

$$\beta_{ij} = (\ddot{z}_i - \ddot{z}_j)(z_i - z_j)$$

It's clear that $\alpha_{ij} = \alpha_{ji}$ and $\beta_{ij} = \beta_{ji}$. Moreover, α_{ij} depends only on the particles positions and velocities in the horizontal plane, while β_{ij} depends also on the accelerations.
In fact, assuming that $\vec{F}_i = \vec{F}_i(\vec{x}_i, \dot{\vec{x}}_i)$ and knowing that $z_i = f(\vec{x}_i)$ and $\dot{z}_i =$

$f_x(\vec{x}_i)\dot{x}_i + f_y(\vec{x}_i)\dot{y}_i$, where x_i and y_i are the horizontal components of $\vec{x}_i$ it can be easily proven that α_{ij} depends just on horizontal positions and velocities. To have a more clear writing, from know on we will follow these assumptions:

$$f_i = f(\vec{x}_i) \qquad z_i = f_i \qquad \dot{z}_i = f_{ix}\dot{x}_i + f_{iy}\dot{y}_i$$

To isolate terms that depend only on the accelerations, we can re-write the 4.3 in the form:

$$\vec{h}_{ij} = -\frac{m_i m_j}{m_i + m_j}\frac{[(\vec{r}_i - \vec{r}_j)}{(\vec{x}_i - \vec{x}_j)\circ(\vec{x}_i - \vec{x}_j)}[\gamma_{ij} + (f_{ix}\ddot{x}_i + f_{iy}\ddot{y}_i - f_{jx}\ddot{x}_j - f_{jy}\ddot{y}_j)(z_i - z_j)] \tag{4.5}$$

Where:

$$\gamma_{ij} = (\vec{x}_i - \vec{x}_j)\cdot(\frac{\vec{F}_i}{m_i} + \frac{\vec{F}_j}{m_j}) + (f_{ix}\dot{x}_i + f_{iy}\dot{y}_i - f_{jx}\dot{x}_j - f_{iy}\dot{y}_i)^2 + (\dot{\vec{x}}_i - \dot{\vec{x}}_j)\cdot(\dot{\vec{y}}_i - \dot{\vec{y}}_j) +$$

$$+(f_{ixx}\dot{x}_i^2 + 2f_{ixy}\dot{x}_i\dot{y}_i + f_{iyy}\dot{y}_i^2 - f_{jxx}\dot{x}_j^2 - 2f_{jxy}\dot{x}_j\dot{y}_j - f_{jyy}\dot{y}_j^2)(z_i - z_j)$$

Gathering some terms together, we can write:

$$M_{ij} = \frac{m_i m_j}{m_i + m_j}$$

$$\Gamma_{ij} = -M_{ij}\frac{\gamma_{ij}}{(\vec{x}_i - \vec{x}_j)\cdot(\vec{x}_i - \vec{x}_j)}$$

$$\Delta_{ij} = -\frac{(z_i - z_j)}{(\vec{x}_i - \vec{x}_j)\cdot(\vec{x}_i - \vec{x}_j)}$$

Thus, the interaction force can be write in the form:

$$\vec{h}_{ij} = (\vec{r}_i - \vec{r}_j)[\Gamma_{ij} - \Delta_{ij}(f_{ix}\ddot{x}_i + f_{iy}\ddot{y}_i - f_{jx}\ddot{x}_j - f_{jy}\ddot{y}_j)] \tag{4.6}$$

M_{ij} and Γ_{ij} are symmetric matrices, while Δ_{ij} is not.

The motion of the two points is described by a linear second−order differential equations system. Introducing:

$$\vec{p}^T = [x_i, y_i, x_j, y_j]$$

$$\vec{b}^T = [F_{ix} + (x_i - x_j)\Gamma_{ij}, F_{iy} + (y_i - y_j)\Gamma_{ij}, F_{jx} + (x_i - x_j)\Gamma_{ij}, F_{jy} + (y_i - y_j)\Gamma_{ij}]$$

we can write the equations in the compact form:

$$A\ddot{\vec{p}} = \vec{b} \tag{4.7}$$

where the mass matrix A is given by:

$$A = \begin{vmatrix} m_i + (x_i - x_j)\Delta_{ij}f_{ix} & (x_i - x_j)\Delta_{ij}f_{iy} & -(x_i - x_j)\Delta_{ij}f_{jx} & -(x_i - x_j)\Delta_{ij}f_{jy} \\ +(y_i - y_j)\Delta_{ij}f_{ix} & m_i + (y_i - y_j)\Delta_{ij}f_{iy} & -(y_i - y_j)\Delta_{ij}f_{jx} & -(y_i - y_j)\Delta_{ij}f_{jy} \\ -(x_i - x_j)\Delta_{ij}f_{ix} & (x_i - x_j)\Delta_{ij}f_{iy} & m_j + (x_i - x_j)\Delta_{ij}f_{jx} & +(x_i - x_j)\Delta_{ij}f_{jy} \\ +(y_i - y_j)\Delta_{ij}f_{ix} & -(y_i - y_j)\Delta_{ij}f_{iy} & (y_i - y_j)\Delta_{ij}f_{jx} & m_j + (y_i - y_j)\Delta_{ij}f_{jy} \end{vmatrix}$$

4.2 Analytical applications

We have solved the system previously described through a MATLAB code, using an RK4 method, as in the previous cases, obtaining a solution for the motion of the sliding particles we can refer to as analytical. Analogously to what was performed in section 3.4, a comparison will be carried out between the solution provided in this way and numerical solutions calculated by means of numerical codes UBO-BLOCK1 and UBO-BLOCK2.
The first one is a code developed by the Tsunami Research Team of the Department of Physis and Astronomy (DIFA) of the Bologna University. It is a 1.5D model for a landlside evolution, based on the same assumptions as UBO-BLOCK2, but with the main difference that the landlside is partitioned into a chain of blocks rather than a matrix of blocks, and that the path of the landslide is prescribed a priori (see the paper [*Tinti et. al.*, 1997, 1999, 2006, 2008; *Lo Iacono et al.*, 2012; *Zaniboni et al.*, 2013; *Zaniboni and Tinti*, 2014] that are some of the several papers showing applications of the model to real and/or realistic scenarios). We further notice that the UBO-BLOCK1 requires as input the undisturbed sliding surface, the initial sliding body, the predefined centre-of-mass trajectory and the lateral boundaries. Theoretically, these factors depend on the landslide evolution, but in many real cases they can be estimated by means of geological considerations. The model UBO-BLOCK1 is written in F77 programming language.

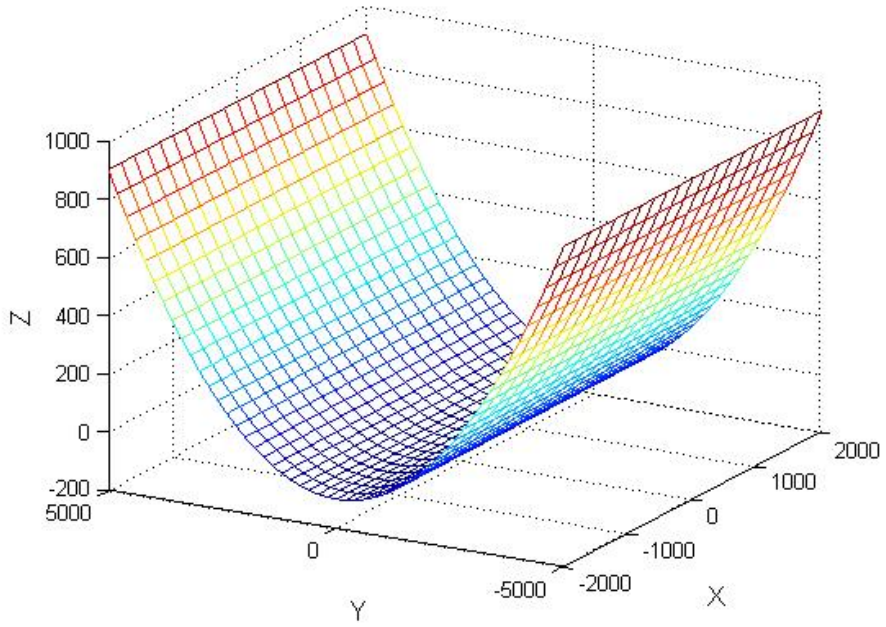

Figure 4.1: Ideal topography described by function 4.8

We have tested the models over an ideal parabolic topography described by a function depending only on the variable y and is uniform n the x direction:

$$z = by^2 - 100 \tag{4.8}$$

where $b = 0.00004$. The slope is shown in figure 4.1. In the first application, we consider two sliding masses, interacting with each other in the sense described in the previous section, and driven by the gravity force. Since the interaction distance-conserving force can be shown to not produce any work over the system, we expect the total system energy to be conserved. Considering a 2-particle system, basically, is like dividing the sliding body in two blocks, which means that the models UBO-BLOCK1 and UBO-BLOCK2, that can treated an arbitrary number of blocks N, are used with a value of N=2.
The grid to represent the surface is built in the intervals $x = [-2000 : 2000]\, m$ and $y = [-5000 : 5000]\, m$ with equal space steps $dx = dy = 200\, m$. In all the simulations the time step is $dt = 0.1\, s$. The starting positions of the two centers of mass are $(x_1 = 0,\, y_1 = -2800)\, m$ and $(x_2 = 0,\, y_2 = -1600)\, m$. In the F77 programs two blocks with height, width and length equal to $20, 400, 1200m$, are defined as the landslide body. We observe that, since the assumed initial positions have the same x coordinate and the sliding surface depend only on y, this case is a mere 1D problem and no transversal motion for the landslide is

expected.

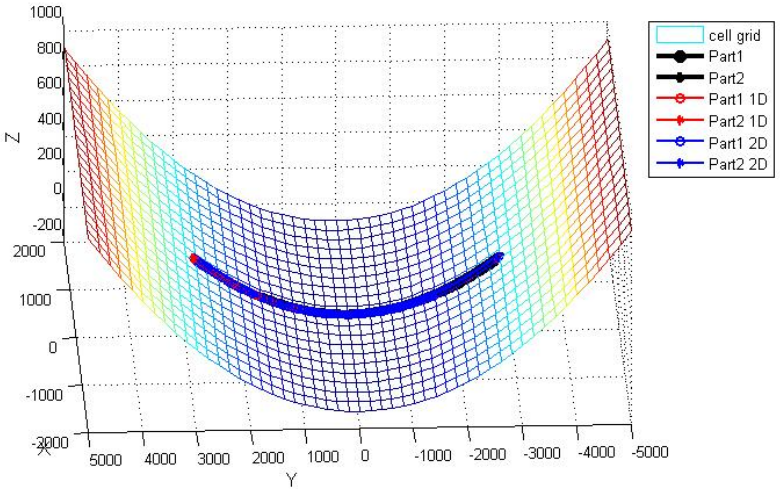

Figure 4.2: Comparison between trajectories from analytical (MATLAB RK4, black), numerical 1D (UBO-BLOCK1, red) and numerical 2D (UBO-BLOCK2, blue) simulation.

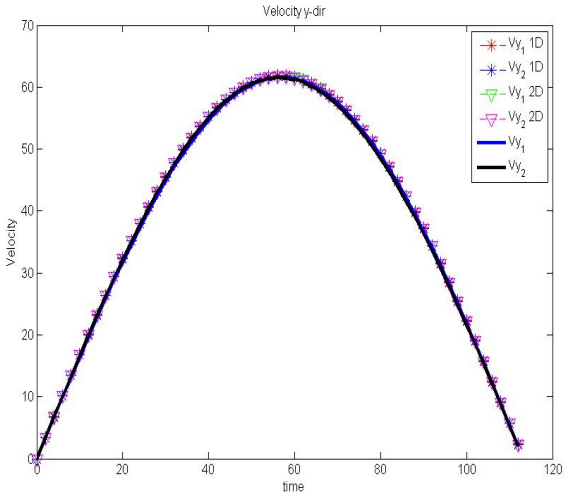

Figure 4.3: Velocity time-histories along the y direction for each mass: analytical (thick blue and black lines), numerical 1D (dashed red and blue lines with asterisks), numerical 2D (dashed green and magenta dashed line with triangles).

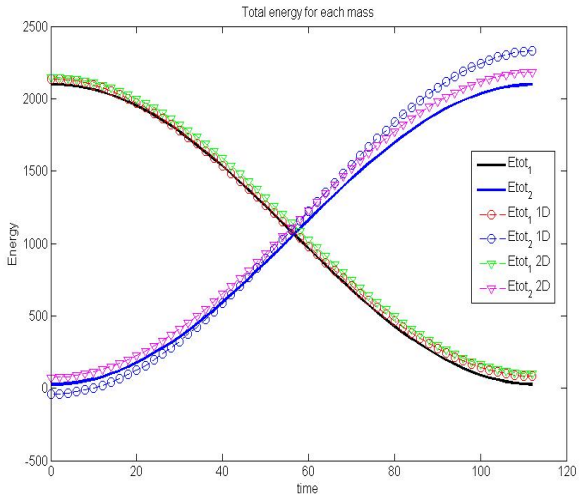

Figure 4.4: Total energy for each mass trends: analytic (thick blue and black line), numerical 1D (dashed red and blue line with open circles, numerical 2D (dashed green and magenta dashed line with open circles).

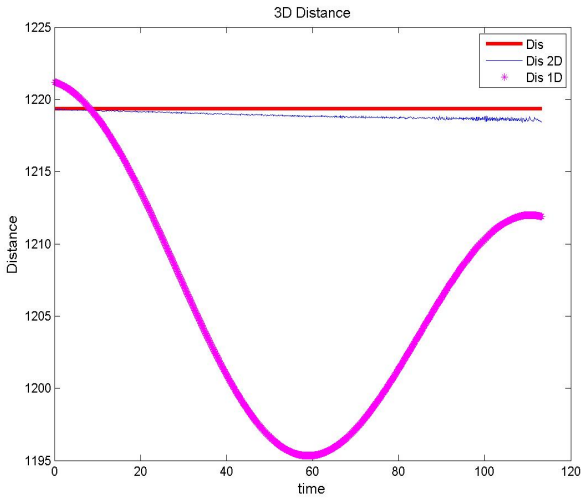

Figure 4.5: Distance changes between the masses: analytical (thick red line), numerical 1D (magenta asterisks), numerical 2D (blue line)

The results of the simulation are shown in figures 4.2 - 4.5. From figures 4.2 and 4.3 it is clear that trajectories and velocities are quite similar. In general

the discrepancy among the analytic and numerical solutions for velocities and trajectories is less then 0.5%. Maximum velocity values are reached at the bottom of the surface ($61.5 - 61.9 m/s$).
Total energy for each mass trends are shown in figure 4.4. We can see some differences among the outputs. These differences are linked to discrepancies in the vertical positions, that is in the z coordinates of the masses. In fact, due to geometrical factors, the initial values of z in the numerical models are slightly different, and this leads to some level of discrepancy also at the following times. As regards the distance between the masses (figure 4.5), we can see that it is well conserved in the analytical solution since this is incorporated in the system of equations, while it is almost conserved in the UBO-BLOCK2 model solution and changes by about 2% in the UBO-BLOCK1 model. It is to be remarked that in both models the interaction forces are computed on a more general basis also allowing for deformations and internal energy dissipation and can be forced at most to conserve distances measured along the trajectories (and not the 3D distances) only indirectly by a specific setting of the basic parameters.

A second test has been carried out on the same topography, but considering the effect of friction forces as well as of buoyancy. We have considered the presence of water in the area of the slope where $z < 0$. Hence, when the blocks go below this level, a mass reduction is applied in order to account for buoyancy effect. This reduction depends on water and rock density ratio ($\alpha_{rid} = 1 - \rho_{sea}/\rho_{rock}$). The assumed friction coefficients values are: $\mu_{dry} = 0.09$ for the subaerial sliding phase and $\mu_{sea} = 0.05$ for the underwater sliding, which are typical values for this problem that can be found in the literature. We also consider a transition belt $z_0 < z < z_1$ ($z_0 = 0\,m, z_1 = -40\,m$) in which the values of masses and μ have intermediate values between the ones of rock and water. For $z*$ belonging to this range, we calculate masses and friction coefficients as:

$$m* = m_0 \left(1 - \frac{z* - z_0}{z_1 - z_0} \left(1 - \alpha_{rid}\right)\right)$$

$$\mu* = \mu_{dry} + \frac{z* - z_0}{z_1 - z_0} \left(\mu_{sea} - \mu_{dry}\right)$$

where m_0 is the value of the block mass outside the water.
In this test, space arrays and initial centers of mass positions are the same as in the previous simulation. Density fraction is set to $\rho_{sea}/\rho_{rock} = 1/3$. Time array is $t = 0 : 136$ for MATLAB code and the UBO-BLOCK2D model stop as well at $t = 136$. UBO-BLOCK1D stop at $t = 147.2$. Time step is equal for every simulation: $dt = 0.1s$.

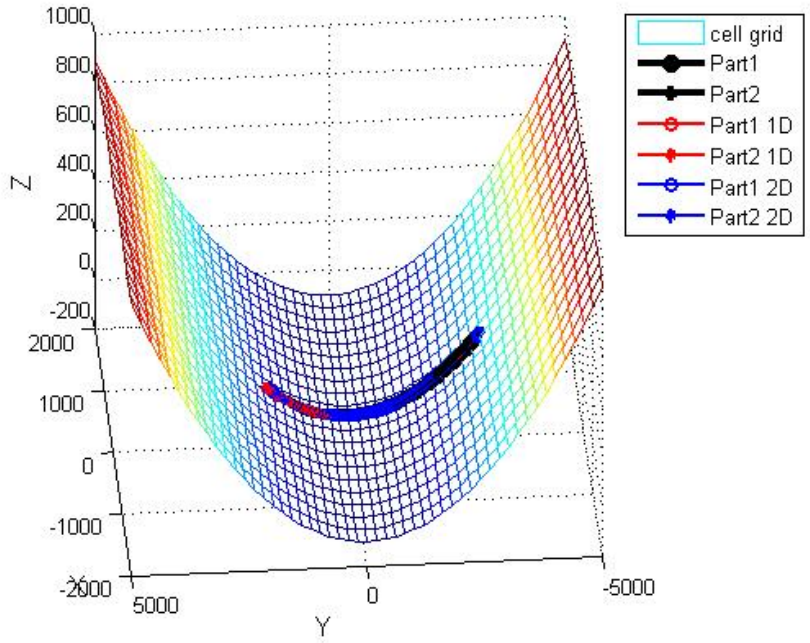

Figure 4.6: Comparison between trajectories from analytical (MATLAB RK4, black), numerical 1D (UBO-BLOCK1, red) and numerical 2D (UBO-BLOCK2, blue) simulation.

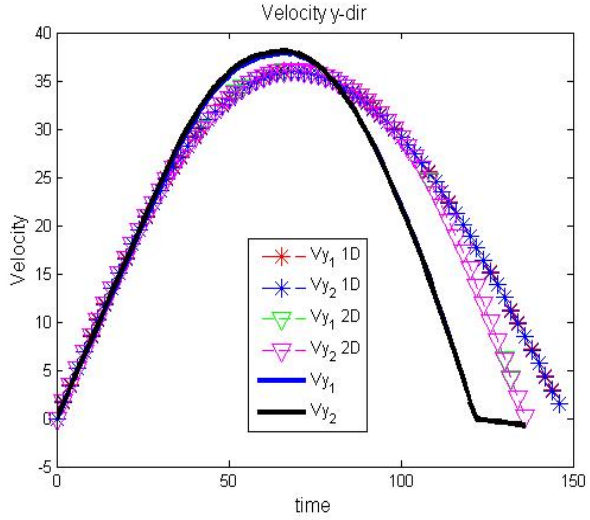

Figure 4.7: Velocity time-histories along the y direction for each mass: analytical (thick blue and black lines), numerical 1D (dashed red and blue lines with asterisks), numerical 2D (dashed green and magenta dashed line with triangles).

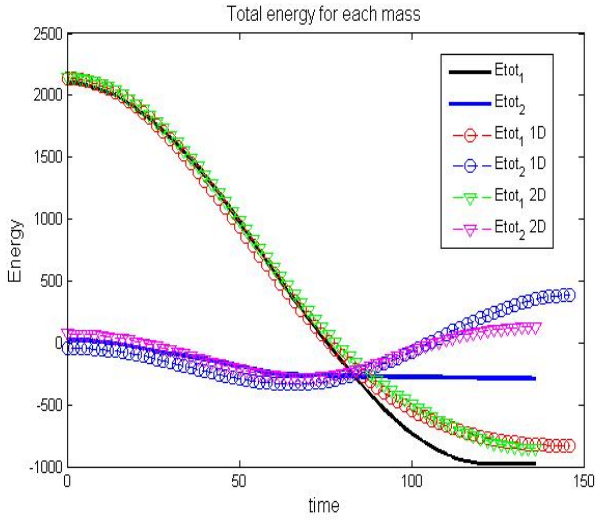

Figure 4.8: Total energy for each mass trends: analytic (thick blue and black line), numerical 1D (dashed red and blue line with open circles, numerical 2D (dashed green and magenta dashed line with open circles).

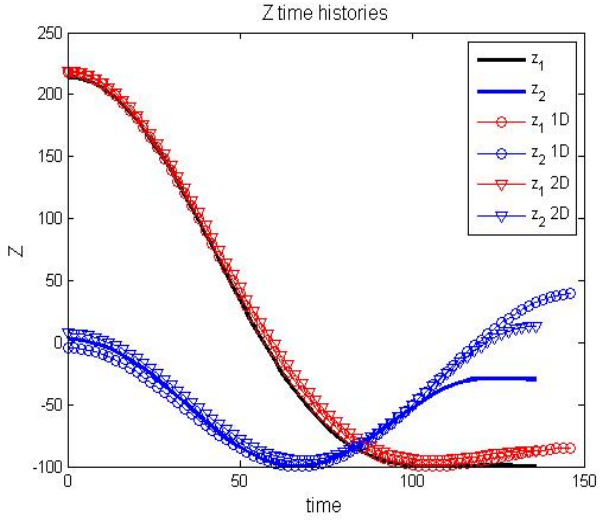

Figure 4.9: Z time-histories for each mass: analytical (thick blue and black lines), numerical 1D (red and blue lines with open circles), numerical 2D (red and blue line with triangles).

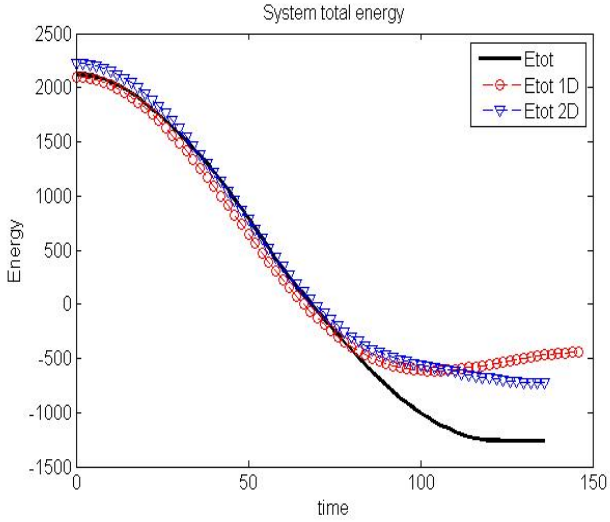

Figure 4.10: Total system energy: analytical (thick black line), numerical 1D (dashed red line with open circles), numerical 2D (dashed blue line with triangles).

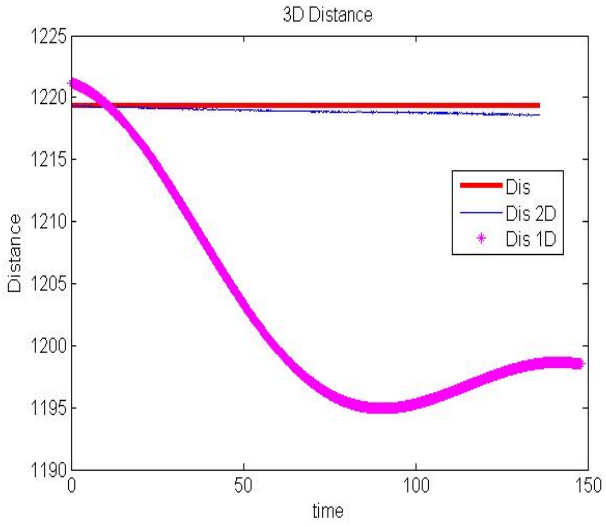

Figure 4.11: Distance changes between the masses: analytical (thick red line), numerical 1D (magenta asterisks), numerical 2D (blue line)

Results are shown in figures 4.6 - 4.11. The trajectories are similar (figure 4.6). Discrepancy in v_y output can be seen. From the analytical output we can deduce that the masses actually stop at the time $t = 120s$. In the numerical 2D time histories the velocities vanish at $t = 140s$, while in the 1D model the masses stop at $t = 147s$. Moreover, the maximum values of velocities are underestimated in both numerical models ($36m/s$ in the numerical, $38m/s$ in the analytical).
Total energy for each mass is shown in figure 4.8. In all trends we see a general energy loss, as expected owing to the presence of dissipative friction forces. Some discrepancies can be noticed after $t = 100s$ due to the different stopping-time in each simulation. In fact, as it can be noticed in the Z time histories 4.9, in the numerical outputs particles reach different values of z in the end.
This difference is clear also in the total system energy trends (figure 4.10) after $t = 90s$. The 3D distance is shown in figure 4.11. Analytical and numerical 2D match almost perfectly, while in the numerical 1D we can see a loss of about 2% as in the previous case.

4.3 Semi-analytical results on Scilla event

In this section we show the results of the application of the MATLAB code to the Scilla region topography. The sliding surface (a regular grid $20\,m$ spaced) has been obtained by interpolating low-resolution data (GEBCO, SRTM public databases and a bathymetry provided by CNR). This provides a not detailed coastline, but is sufficient for the purposes of this work. Due to the strong

geometrical irregularity in the sliding area, the contour has been smoothed to reduce code numerical instabilities. The smoothed topography is shown in the next figure:

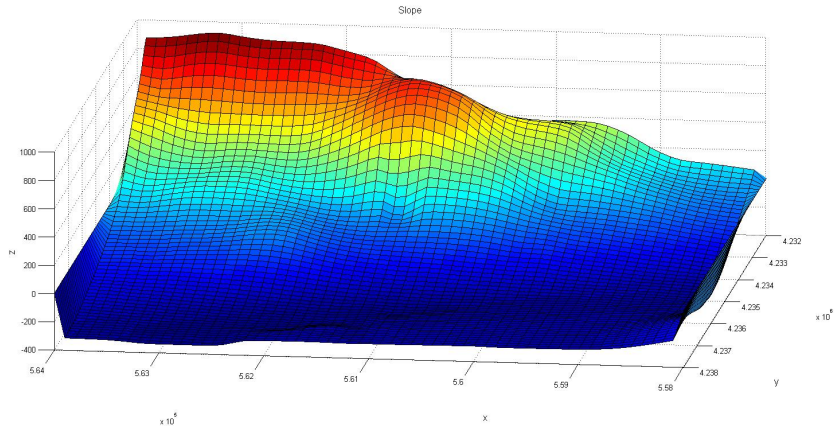

Figure 4.12: Smoothed topography of Scilla region.

The dynamics is fully described by equations 4.7, solved through the RK4 method described in section **??**. Moreover, we consider also the buoyancy force due to the presence of the water. Water and rock density ratio is set as:

$$\rho_{sea}/\rho_{dry} = 1/3 \qquad \mu_{dry} = 0.4 \;\; \mu_{sea} = 0.1$$

The initial positions, given in UTM coordinates, are set in:

$$x_1 = 561323 \qquad y_1 = 4233578$$

$$x_2 = 561249 \qquad y_2 = 4234015$$

The time array is $t = 0 : 150s$ and time step is $dt = 0.5s$. To have a better understanding of the whole landslide system, the results are shown in terms of the center of mass of the two particles.

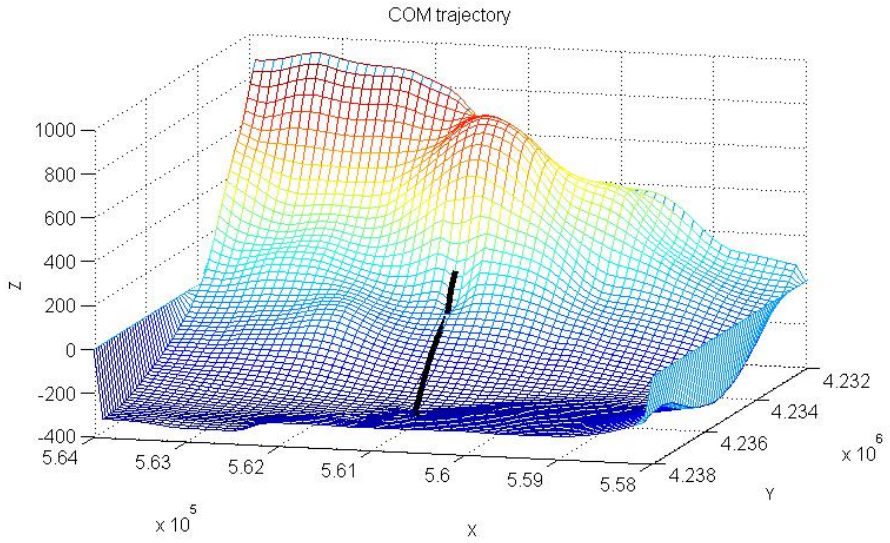

Figure 4.13: Center−of− mass trajectory .

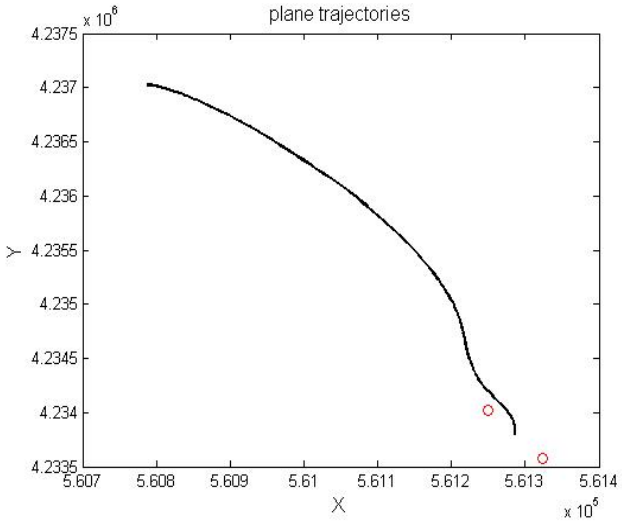

Figure 4.14: Center− of − mass plane trajectory (black thick line). The two initial points are shown in open red circle.

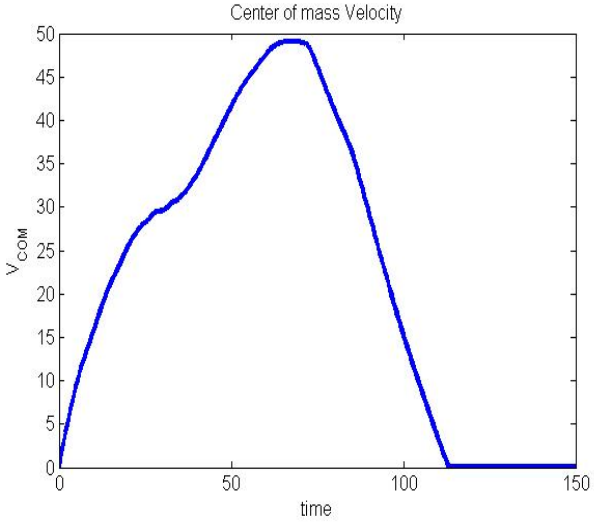

Figure 4.15: Center − of − mass velocity .

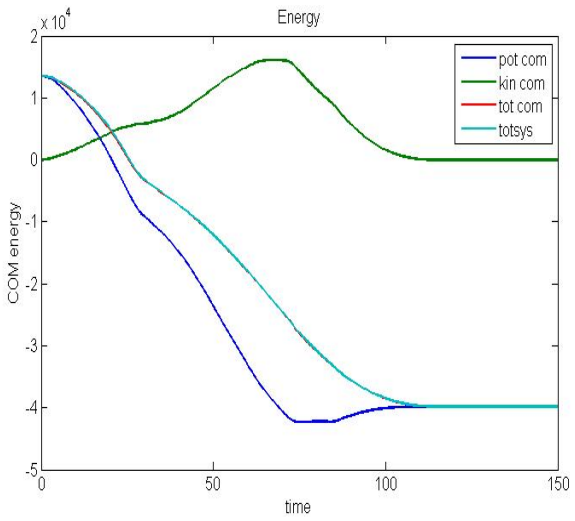

Figure 4.16: Energy trends: COM potential energy (blue line), COM kinetic energy (green line), COM total energy (red line), total system energy (cyan line)

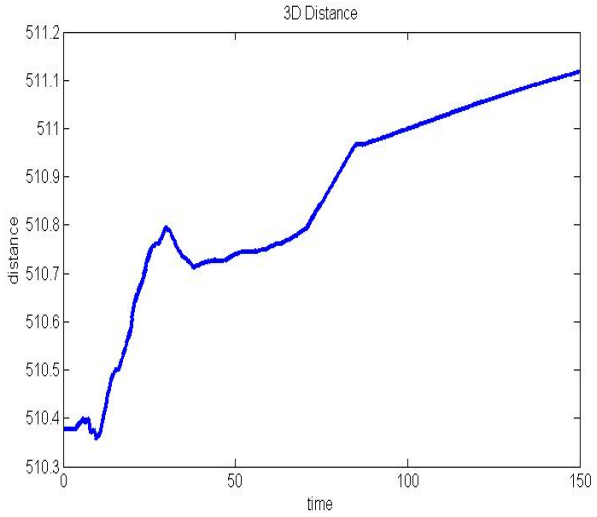

Figure 4.17: 3D distance among the two particles.

Results are shown in figures **??**- 4.17. COM velocity maximum is about $48m/s$ (figure 4.15). Moreover, the COM velocity plot suggests us that the the center-of-mass enters in the water approximately at $t = 30s$. The landslide stops at $t = 110s$ where velocity became constant and equal to zero.
Energy graphs (COM kinetic,COM potential, COM total and total system) are shown in figure 4.16. Kinetic energy reaches a maximum when the velocity reaches higher value, as we expected. Potential energy shows a general loss since the landslide is moving downward. The total system energy overlaps the COM total energy, as we expected, showing a general loss due to the presence of dissipative forces.
The distance is conserved, whit small fluctuations (figure 4.17).

4.4 Numerical results on Scilla event

The simulation of the 1783 Scilla landslide has been run by means of the UBO-BLOCK1 numerical code . A topography and bathymetry composed by the same grid of the previous section is been used.

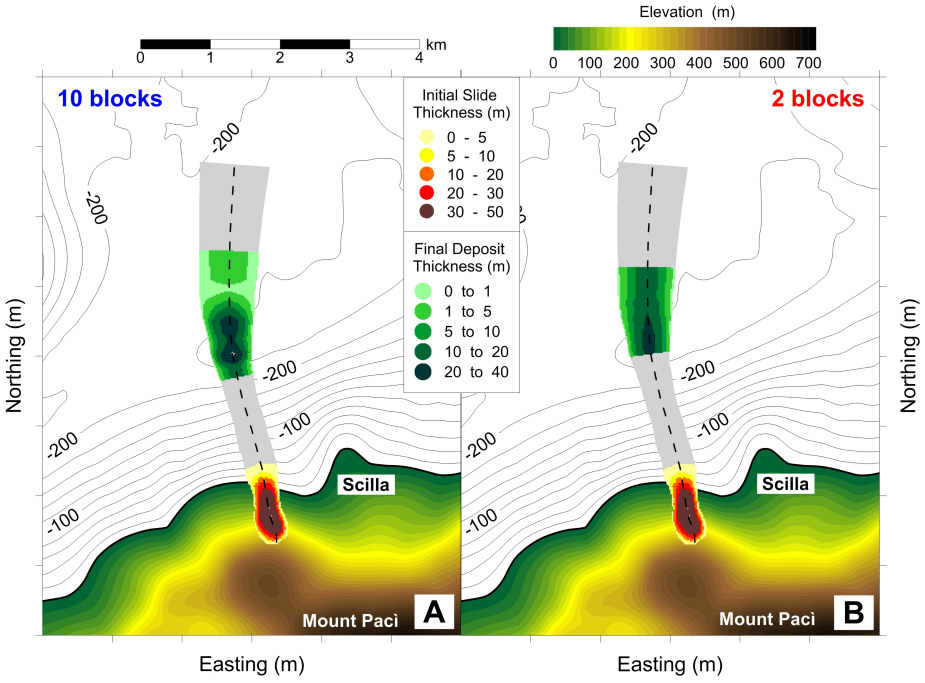

Figure 4.18: Map of the 1783 Scilla landslide, with in evidence the initial slide thickness (yellow-red-brown scale), the centre of mass trajectory (black dashed line) and the area covered by the slide motion (light grey). Panel A reports the final deposit (green scale) for the 10-blocks simulation, Panel B the 2-blocks mass subdivision.

The sliding body, marked by the yellow-red-brown-scale area accounting for the initial thickness, is reconstructed by considering the worst case for the 1783 collapse, i.e. a subaerial-submarine mass detaching from Mount Pací from almost $400\,m$ a.s.l. down to $50\,m$ sea depth. This results into a mobilized volume of $9.4\,10^6 m^3$, higher than the volume hypothesized by other authors, that considered only a subaerial portion by means of morphological considerations [*Bozzano et al.*, 2011; *Mazzanti and Bozzano*, 2011). As can be noticed in 4.18, the maximum thickness ranges $50\,m$, with an average value of $20\,m$.
The centre of mass trajectory (marked by the black dashed line in figure 4.18 has been chosen following the maximum local gradient and by considering the location of some submarine deposit associated with the 1783 event [*Bozzano et al.*, 2011), at about $250\,m$ depth; the slide underwater lateral spreading is accounted for by the light-grey area in figure 4.18.
As we have seen, the numerical code UBO-BLOCK1 has been applied by taking into consideration two possible initial configurations: the sliding mass has been divided into 10 and into 2 blocks, the remaining parameters (basal friction, drag, interaction coefficient) maintained the same. This procedure has been adopted in order to discern the influence of the number of subdivisions of

the initial mass on the simulated slide dynamics and on the generated tsunami. Figure 4.18 shows the position and the distribution of the final simulated deposit for the 10-block case (panel A) and for the 2-block one (panel B). We can notice that the main deposit thickness (up to $40\,m$) concentrates on the deeper area, around $250\,m$ b.s.l., the sliding body maintaining almost unchanged its longitudinal extension along the sliding direction.

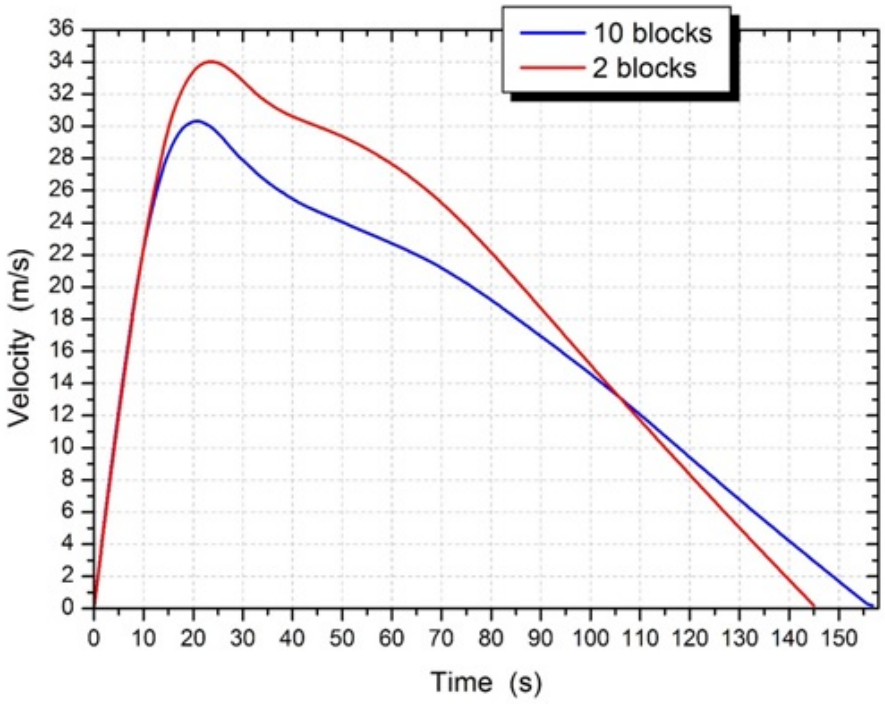

Figure 4.19: Velocity time histories for the two considered initial configurations of the Scilla slide: 10-blocks (blue line) and 2-blocks (red line). The velocity here shown is computed as the average of the single blocks velocity.

Concerning the dynamics, the numerical code provides also the velocity at each time step, necessary to evaluate the tsunami impulse. As can be seen in Figure 4.19, the velocity follows the typical trend for slides along continental margins [*Zaniboni et al.*, 2014]: an initial strong acceleration phase brings the mass to velocities ranging $30m/s$ for the 10-block case, and $34m/s$ for 2-blocks, corresponding to the motion in steepest slopes, in around 20 seconds. After this, a slow deceleration phase occurs, corresponding to the motion in milder bathymetry and in presence of the water. The two simulations show very similar

dynamics, even if the 2-block one reaches higher values (about 10% more), this effect accounting for the lower number of blocks, meaning less energy dispersion due to internal interaction.

4.4.1 Tsunami generation

The movement of the mass on the sea bottom causes the displacement of the sea surface, that begins to oscillate propagating the perturbation. The generated tsunami wave is here simulated via the numerical code UBO-TSUFD, developed by the University of Bologna Tsunami Research Team as well, adopting a finite difference technique to solve the Navier-Stokes equations in shallow water approximation: in this application they have been solved in their linear expression, using a staggered grid scheme. Further details on the model and some applications can be seen in [*Tonini et al.*, 2011 and *Tinti and Tonini*, 2013]. The impulse provided by the sliding mass is introduced as a forcing term in the hydrodynamical equations, and is computed at each time step of the sliding motion by filtering it with the sea depth, and interpolating it on the tsunami computational grid. These tasks are performed by the intermediate code UBO-TSUIMP. The code requires as input a regular grid, accounting for the bathymetry (for wave propagation) and topography (for land inundation) of the studied area. In this application, the focused area is the near-field, and especially the coastline close to Scilla, where most of the casualties were registered.

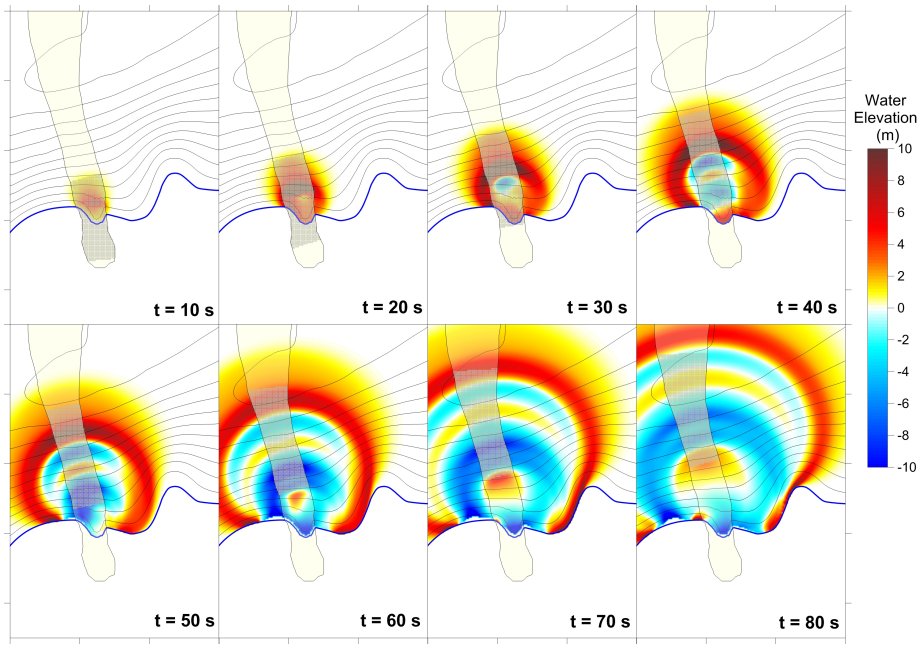

Figure 4.20: Tsunami propagation over the computational domain. Sea level rise is marked in yellow-red, sea withdrawal in cyan-blue. The pale yellow area marks the sliding surface boundary, in light grey the positions of the slide at the different time steps are reported.

The propagation of the tsunami (here the 10-block case) is shown in Figure 4.20, at different time steps. It first manifests as a positive signal, meaning sea level rise, followed by an almost radial propagation form the source area (see also the $t = 20\,s$ sketch). After this, the interaction with the bathymetry and the coast deforms the wave, while into the open sea, northward, the tsunami propagates with a main circular positive front of some meters. The Scilla coastline is hit by a sea level rise of $6-8\,m$ after around one minute ($t = 60-70\,s$ sketches): at this stage it is already evident the sequence of sea level rise-retreat, marked by the yellow-red and cyan-blue areas respectively. Notice also that only after $80\,s$ the tsunami front begins to distance itself from the sliding mass (whose evolution is marked in light grey in the sketches), meaning that for the previous phase they move with similar velocities, reaching the resonance conditions that provides the maximum energy transfer from the mass to the wave.

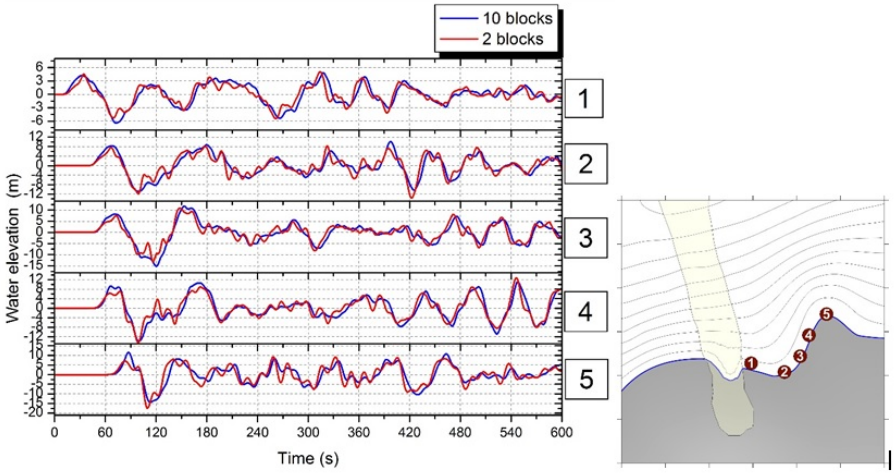

Figure 4.21: Virtual marigrams computed on 5 points along the coastline, which location is shown on the right. The tsunami generated by the 10-blocks (blue) and 2-blocks (red) cases are reported.

Synthetic marigrams positioned close to the source and along the Scilla coastline (Figure 4.21, right panel), show the comparison between the 10-block and 2-block cases: in both cases, a first positive wave hits the coast, rising over up to$10\,m$ almost everywhere, in full compatibility with historical reports. A long series of oscillations characterize the coastal stretch with a period ranging 1 minute. The first wave is not necessarily the highest one (see for example marigram 4). The sea level oscillations provided by the two slide simulations are almost superimposed, apart from some higher frequency oscillations characterizing the 2-block case.

4.5 Comparison between semi-analytical and numerical results

Comparing the analytical and numerical results shown in the previous sections we can notice some differences in the velocity plots. (Figure 4.15 and Figure 4.19). The maximum values reached are different: $48m/s$ in the analytical output, $34m/s$ in the numerical simulation with 2 blocks and $30m/s$ in the numerical results with 10 blocks. Moreover, the general curves are different: the numerical outputs show a general decrease− phase for $t > 30\,s$, while in the analytical one the velocity growth-phase terminates at $t = 70\,s$. On the other hand, the decreasing occurs rapidly in the analytical graph, while in the numerical one we can notice a slower decline. This discrepancy is due to the absence of drag forces in the analytical program. This kind of forces act opposite to any mass moving with respect to a surrounding fluid (in this case air or water).

Unlike other resistive forces, such as dry friction, which are nearly independent of velocity, drag forces depend on it and lead to a general velocity decrease. Anyway, all codes applied to the 1783 Scilla landslide show that the sliding body reached high velocity in short time (over $30 m/s$ in about 30 seconds).
From the numerical simulations we deduce that the generated tsunami reaches the coast of Scilla in about 1 minute, with a considerable sea level rise, up to $8-10$ meters, fully compatible with the historical reports. After the first arrival, a series of oscillations affect the coast for many minutes, with dominant period around 1 minute. A sensitivity analysis on the effect of 10-block vs. 2-block initial mass subdivision shows that the maximum velocity change ranges within the 10%, while the discrepancy between the corresponding tsunamis is almost negligible, the 2-block wave showing higher frequency disturbances.

Conclusions

In this thesis we have shown the development of a semi-analytic model to calculate the motion of sliding particles over a surface.
In the first part of this work a detailed study has been conducted on the mathematical characteristics of the model. Studies on derivatives discretization and interpolation over arbitrary points of a grid in a Cartesian reference system suggest us that smoothed geometries are more suitable to these processes and lead to more reasonable results.
Furthermore, several applications of the semi-analytical model and comparison with Lagrangian numerical models of landslide evolution have been carried out. The cases of single particle motion allow us to show the model behavior over very different shapes, providing very consistent results in all ideal scenarios. The comparisons helped us to understand numerical model weaknesses facing particular sliding surface geometries. Even in this case we have proven that strong geometry irregularities (such as rapid changing in slope gradient) are the main source of errors.
Another set of applications has been carried out considering the interacting force between two sliding particles. It has to be outlined that the formal description of the interaction force leads to several kinds of mathematical and computational issues that cannot be avoided in some cases. To solve the linear second-order differential equations system that describes the motion of the particles, we need the inverse of the mass matrix A. This process is not always possible due to numerical instabilities and in some cases can produce non-realistic system solutions. A detailed study on the stability of this particular system was not performed. Further studies could bring a more comprehensive pattern of initial conditions that ensures stability. Anyway, the applications on ideal surfaces have shown appropriate results. Comparison with numerical models has shown very good results despite they adopt different parametrization of the interaction forces.
Clearly, the main core of this work is the model application to the Scilla 1783 event and the subsequent comparison with results obtained by means of the UBO-BLOCK1 numerical code. This comparison is essential to prove the effective working value of the MATLAB code. The landslide body has been divided in 2 and 10 blocks in order to show that this a-priori assumption does not determine strong differences in the model output. In particular, since the 2-block- and the 10-block-model runs provide consistent results for the tsunami genera-

tion, we can deduce that an analytical description of the landslide based on just two main centers of mass is actually a satisfactory first-level approximation. In fact, it has to be outlined that the numerical model has the potential to describe in more details the geometries and kinematics of a complex sliding body, while in the analytical approach we describe the landslide system with just two points, that keep their distance constant during their motion on the surface.

Bibliography

[1] Abramson L.W., T.S.Lee, S. Sharma, G.M.Boyce
Slope stability and stabilization,
2002,736p. , John Wiley & son's, New York

[2] Roy C. Sidle,Hirotaka Ochiai.
Landslides : processes, prediction and land use.
American Geophysical Union, 2006

[3] Bechini C.
Natural conditions controlling earthflows occurrence in the Eden Canyon area(S. Francisco bay, California)
1993,Z.Geomorph. N.F.,91-105

[4] Boore D.M.
The effect of simple topography on seismic waves: implications for the acceleration recorded at Pacaoima Dam, San Fernando Valley, California
1973, Bull. Seismol. Soc. Am. ,1603-1609

[5] Bosman A., Bozzano F., Chiocci FL., Mazzanti P.
The 1783 Scilla tsunami: evidences of a submarine landslide as a possible cause.
2006, Geophysical Research Abstracts, 8, p 10558

[6] Bortolucci Elisabetta
Modelli dinamici di frane e dei maremoti indotti
2001, Phd. Thesis.

[7] Boschi E., Guidoboni E., Ferrari G., Mariotti D., Valensise G., Gasperini P.
Catalogue of strong Italian earthquakes from 461 b.C. to 1997.
2000, Ann. Geofis., 43:609–868

[8] Bozzano F. , Lenti L. ,Martino S., Montagna A. ,Paciello A. .
Earthquake triggering of landslides in highly jointed rock masses: Reconstruction of the 1783 Scilla rock avalanche 2011, Geomorphology

[9] Bozzano F., Martino S., Mazzanti P. ,Montagna A., Prestinizi A.
The 1783 Scilla rock avalanche (Calabria, Southern Italy) 2008, Proceeding of the 10th international symposium on landslides and engineered slopes.

[10] Brunsden D.
Landslide types, mechanism, recognition,identification
1985,"Landslide in the South Wales Coalfield", C.S.Morgan, Polytech. of wales, UK.

[11] Brunsden D. and D.B.
Slope Instability
1984, John Wiley & Sons, Chichester, UK.

[12] Caine N.
Summer rainstorms in an alpine environments and their influence on soil erosion, San Juan Mountains, Colorado
1976, Archt. Alp. Res, 183-196

[13] Campbell A.P.
Measurement of movement of an earthflow
1966, Soil Water, 23-24

[14] Coe. J.A., Ellis W.L., Godt J.W., Savage J.E., Michael J.A., Kibler J. D.
Seasonal movement of the Slumgullion landslide determined from GPS surveys and fields instrumentation, July 1998
2002, Eng. Geol. , 67-101

[15] Cornfoth, D.H.
Landslides in Practice: investigation, Analysis, Remedial Prevention option in soils
2005, John Wiley and sons , New York.

[16] Cruden D.M. and Varnes
Landslide types and processes
1996,"Landslides-Investigation and mitigation", edit by A.K. Turner and R.L.Schuster, National Academic Press , Washington, DC.

[17] De Lorenzo A.
Moemorie da servire alla storia sacra e civile di Reggio e delle Calabrie
1887, Cronache e Documenti inediti o rari, bol I.

[18] Dikau R., Brundsden D., Ibsen M.L., Schroot L.
Landslide recognition: identification, movement and causes
1996, John Wiley and sons, Chichester, UK.

[19] Eisbacher G.H.
Slope stability and land use in mountain valleys
1982, Geoscience Canada, 14-27.

[20] Furaya G., Sassa K., Hiura H., Fukuoka H.
Mechanism of creep movement caused by landslide activity and underground erosion in crystalline schist, Shikoku Island, southernwestern Japan
1999, Eng. Geol., 311-325.

[21] Gao J.
Identification of topographic settings conductive to landsliding from DEM in Nelson Country
1993, Earth. Surf. Process.Landforms, 579-591.

[22] Gerardi F., Barbano MS., De Martini PM, Pantosi D.
Discrimination of tsunami sources on the basis of historical data in esatern Sicily and southern Calabria
2008, Bull seismol. soc. am.

[23] Graziani L., Maramai A., Tinti S.
A revision of the 1783–1784 Calabrian tsunamis.
2006, Nat. Hazards Earth System Sci

[24] Gupta R.P., Joshi B.C.
Landslide hazard zoning using the GIS approach-a case study from the Ramganga Catchment, Himalayas
1990, Eng. Geol., 119-131.

[25] Hamilton W
Relazione dell'ultimo terremoto delle Calabrie e delle Sicilia
1783.

[26] Harp E., Wilson L.C., Wieczorek G.F.
Landslides from the February 4, 1976, Guatemala earthquake
1981, Prof.Pap., U.S. Geol. Surv.

[27] Harper S.B.
Use of approximate mobility index to identify areas susceptible to landsliding by rapid mobilization to debris flows in souther Thailand
1993, J. Southeast Asian Earth. Science, 587-596.

[28] Hough B.K.
An analysis of the effect of particle interlocking on the strength of cohesionless soils
1951, Am. Soc. Testing and materials Bull. 176.

[29] Howes D.E., Kenk E.
Terrain classification system for British Columbia
1988, Ministry of Crown Lands, Victoria, BC, Canada.

[30] Ives J.D., Messerli B.
Mountain hazards mapping in Nepal. Introduction to an applied mountain research project
1981, Mountain Res. Develop. 223-230.

[31] Keefer D.K., Wilson R.C., Mark R.K., Brabb E.E., Brown W.M., Ellen S.D., Harp E.L., Wieczorek G.F., Alger C.S., Zatkin R.S.
Real time landslide waring during heavy rainfall
1987, Science. 921-925.

[32] Khazai B., Sitar N.
Evaluation of factors controlling earthquake induced landslides caused by Chi-Chi earthquake and comparison with the Northridge and Loma Prieta events
2003, Eng. Geo., 79-95.

[33] Kienholtz H., Scheineider G., Bischel M., Grunder M., Mool P.
Mapping of mountain hazards and slope stability
1984, Mountain. Res. Develop., 247-266.

[34] Larsen M.C., Simon A.
A rainfall intensity-duration threshold for landslides in a humid-tropical environment, Puerto Rico
1993, Geograf. Ann., 13-23.

[35] Li T., Li M.
A preliminary study on landslide triggered by heavy rainfall
1985, Int. Symp. on Erosion, Debirs flow and disaster prevention. Tsukuba, Japan.

[36] Lo Iacono C., Gracia E., Zaniboni F., Pagnoni G., Tinti S., Bartolomé R., Masson D., Wynn R., Lourenco N., Pinto de Abreau M., Danobeitia JJ., Zitellini N.
Large and deep slope failures in the Gorringe Bank: Evidence for landslide-generated tsunamis along the SW Iberian Margin
2012, Geology 40: 931-934. doi: 10.1130/G33446.1

[37] Mazzanti P.
Studio integrato subaereo–subacqueo di frane in ambiente costiero: i casi di Scilla e del lago di Albano
2008, Giornale di Geologia Applicata.

[38] Mazzanti P., Bozzano F.
Revisiting the February 6th Scilla (Calabria,Italy) landslide and tsunami by numerical simulation
2011, Mar Geophys Res DOI 10.1007/s11001–011–9117–1.

[39] Mazzanti P., Bozzano F., Avolio MV, Lupiano V., Di Gregorio S.
3D numerical modelling of submerged and coastal landslides propagation.
2009, The Netherlands, pp 127–139

[40] Miller J.D.
Coupling GIS with physical models to assess deep-seated landslide hazards.
1995, Envir. Eng. Geosci., 263-276.

[41] Minasi A.
La specola del filosofo
1970, "Natura e sorti nelle incisioni di Antonio Minasi", Ilario Principe, "Brutium".

[42] Minasi G
Continuazione ed appendice sopra i tremuoti descritti nella relazione 468 colla data di Scilla de 30 settembre 1783 con altro che accadde in progresso, 469 Messina.
1785.

[43] Murphy W.
The geomorphological controls on seismically triggered landslides during the 1908 Straits of Messina earthquake, southern Italy.
1995, Q.J. Eng. Geol., 61-74.

[44] Nishimura K., Morii
An observed effect of topography on seismic ground motions
1983, Jisin, 383-392.

[45] Ocakoglu F., Gokceoglu C., Ercanoglu M.
Dinamics of a complex mass movement triggered by heavy rainfall: a case study from NW Turkey
2002, Geomorphology, 42, 329–341

[46] Ochiai H, Matsuura S., Yanase H.
Pore pressure change in soil layer of a landslide area during earthquake
1987, Proc. 5th Conf. and field workshop on landslides, 205–210

[47] Okunishi K., Sonoda M., Yokoyama K.
Geomorphic and environmental controls of earthquake-induced landslides.
1999, Trans. Jpn. Geomorph. Union, 3, 41–56

[48] Pachauri A.K., Pant M.
Landslide hazard mapping based on geological attributes.
1992, Eng- Geol.., 32, 81–100

[49] Palacios D., Garcia R., Rubio V., Vigil R.
Debris flows in a weathered grantic massif: Sierra de Gredos, Spain.
2003, Catena, 51, 115–140

[50] Rahn P.H.
The relationship between natural forested slopes and angles of repose for sand and gravel.
1969, Geol. Soc. Am. Bull, 80, 2123–2128

[51] Rohn J., Fernandez–Steeger T., Sidow D., Czurda K.
Rock fall triggers earthflow by undrained loading at Steinbach, Austria, April 1995.
2003, landslide News, 14–15, 33–35

[52] Sarconi M.
istoria de fenomeni del tremuoto avvenuto nelle Calabrie, e nel Valdemone nell'anno 1783.
1784, Reale accademia delle scienze e delle belle lettere di Napoli.

[53] Sasaki Y., Fujii A., Asai K.
Soil creep process and its role in debris slide generation
2000, Eng. Geol., 56, 163–183

[54] Shoaei Z., Ghayoumian J.
Seimareh landslide, western Iran, one of the worlds largest complex landslides.
2000, Landslide neews, 13, 23–26

[55] Sidle R., Dhakal S.
Potential effects of environmental change on landslide hazards in forest environments.
2002, Environmental Change and Geomorphic hazard in forest, 136–165.

[56] Sidle R., Dhakal S.
Stability of natural slopes and embankment foundation.
1969, Proc. 7th Int. Conf. Soil Mech. Found. Eng. , 3, 291–340, Mexico.

[57] Sonoda M.
A numerical simulation of displacement of weathred granite on a forest slope.
1998, Trans. Jpn. Geomorph. Union, 19, 135–154

[58] Swanston D. N.
Mass wasting in coastal Alaska
1969, Res Paper, PNW 83, 15 p.

[59] Swanston D. N. and Swanston F.J.
Timber harvesing, mass erosion, and steepland forest geomorphology in the Pacific Northwest.
1976, Geomorphology and Engineering.

[60] Tang C., Grunert J.
Inventory of landslides triggered by the 1996 Lijiang Earthquake, Yunnan Province, China.
1999, Trans. Jpn. Geomorph. Union, 20, 335–349.

[61] Tinti S. , Piatanesi A.
Finite element simulations of the 5 February 1783 Calabrian tsunami
1997, Phis. chem. earth.

[62] Tinti S., Bortolucci E., Armigliato A.
Numerical simulation of the landslide-induced tsunami of 1988 on Vulcano Island, Italy.
1999, B Volcanol 61: 121–137.

[63] Tinti S., Bortolucci E., Romagnoli C.
Computer simulations of tsunamis due to flank collapse at Stromboli, Italy
Journal of Volcanology and Geothermal Research, 6, 103-128., 2000

[64] Tinti S., Bortolucci E., Vannini C.
A block-based theoretical model suited to gravitational sliding
1997, Nat Hazards 16: 1–28

[65] Tinti S., Pagnoni G., Zaniboni F., Bortolucci E.
Tsunami generation in Stromboli Island and impact on the south-east Tyrrhenian coasts
2003, Natural Hazards and Earth System Sciences, 3, 299-309.

[66] Tinti S., Pagnoni G., Zaniboni F.
The landslides and tsunamis of the 30th of December 2002 in Stromboli analysed through numerical simulations
2008, B Volcanol 68: 462–479. doi: 10.1007/s00445–005–0022–9.

[67] Tinti S., Pagnoni G., Zaniboni F., Manucci A.
Stromboli Island (Italy): scenarios of tsunamis generated by submarine landslides
2008, Pure Appl Geophys 165: 2143–2167. doi: 10.1007/s00024–008–0420–y.

[68] Tinti S., Zaniboni F. *Lagrangian 1D and 2D models for the simulation of the Vajont landslide, October 9th, 1963, Italy* 32nd International Geological Congress, Firenze, 20-28 Agosto 2004, abstract and poster n. 103-25, 2004

[69] Turner A.K., Schuster
Landslides- Investigation and Mitigation.
1996, Special report 247, trans. Res. Board, National Res. Council.

[70] Vivienzo G.
Istoria de trmuoti avvenuti nella provincia di Calabria ulteriore e nella citta di Messina nell'anno 1783
1788, Napoli.

[71] Wentworth C.K.
Soil avalanches on Oahu, Hawaii
1943, Geol. Soc. Am. Bull., 54, 53–64.

[72] Wu T. and Sangrey A.
Strength properties and their measurement
1978, Landslides: analysis and control, special rep. 176, pp 139–154.

[73] Wu W., Sidle R. C.
A distributed slope stability model for steep forested hillslopes
1995, Water Resour. Res. 31, 2097–2110.

[74] Zaniboni F., Pagnoni G., Tinti S., Della Seta M., Fredi P., Marotta E., Orsi G.
The potential failure of Monte Nuovo at Ischia Island (Southern Italy): numerical assessment of a likely induced tsunami and its effects on a densely inhabited area
2013, Bull.Volcanol., 75, 11, 763, DOI 10.1007/s00445–013–0763–9.

[75] Zaniboni F., Tinti S.
Numerical simulations of the 1963 Vajont Landslide, Italy: Application of 1D Lagrangian Modelling
2014, Natural Hazards, 70, 567-592, doi: 10.1007/s11069-013-0828-2.